Biophysical Insights into ZnO and Carbon Nanodot-Plant Interactions through Impedance Spectroscopy of Crassula ovata

Kajal Gautam

gautamkajal1210@gmail.com

UPES https://orcid.org/0000-0002-2427-7229

Mohit Bhatt

UPES

Archna Sagdeo

HBNI

Anil Sinha

UPES

Hukum Singh

Forest Research Institute https://orcid.org/0000-0003-2112-6182

Article

Keywords: Crassula ovata, carbon nanodots (CND), ZnO nanoparticles, impedance spectroscopy, plant nanobionics, biophysics, charge transport

Posted Date: October 14th, 2025

DOI: https://doi.org/10.21203/rs.3.rs-7837159/v1

Additional Declarations: There is **NO** Competing Interest.

Biophysical Insights into ZnO and Carbon Nanodot-Plant Interactions through Impedance Spectroscopy of *Crassula ovata*

Kajal Gautam[1*], Mohit Bhatt[2], Archna Sagdeo[3], Anil Kumar Sinha[2*], Hukum Singh[4]

[1]Department of Chemistry, School of Advanced Engineering, UPES, Dehradun, India, 248007
[2]Department of Physics, School of Advanced Engineering, UPES, Dehradun, India, 248007
[3]Homi Bhabha National Institute, Training School Complex, Anushakti Nagar, Mumbai, India 400094
[4]ICFRE-Forest Research Institute, PO New Forest, Dehradun, India, 248006
Corresponding address: gautamkajal1210@gmail.com (Kajal Gautam) and anilksinha11@gmail.com (Anil Kumar Sinha)

Abstract

Insertion of nanoparticles (NPs) in plants induce various biophysical changes as well as modulate ion channels and transporters, resulting in improved water and nutrient uptake. High concentration of NPs has toxic effect like excessive production of reactive oxygen species, hormonal imbalances and impaired cellular processes. These biophysical changes also change the complex impedance of plant leaves. Here, we use impedance spectroscopy to probe, for the first time, the electrochemical response of the succulent *Crassula ovata* leaves following exposure to water-soluble carbon nanodots (CNDs) and zinc oxide (ZnO) nanoparticles. Nanoparticles were introduced through static root immersion in aqueous suspensions at varying concentrations (1, 5, and 10 mg L^{-1}). Quantitative analysis revealed strikingly different dielectric signatures. CND treatment caused grain boundary (gb) resistance to rise from ~256 Ω in the control sample to ~27.6 kΩ at 10 mg L^{-1} accompanied by a consistent suppression of permittivity, reflecting progressive obstruction of ionic pathways and space-charge accumulation, on NP insertion. ZnO NPs, in contrast, showed a saturation effect: gb resistance peaked at ~14.6 kΩ at 5 mg L^{-1} but declined to ~7.3 kΩ at 10 mg L^{-1}, where conductivity and dielectric relaxation partially recovered through Zn^{2+}-mediated defect pathways. Equivalent-circuit modelling and Jonscher analysis corroborated these concentration-dependent shifts, revealing nanomaterial-specific modulation of ionic mobility and capacitive behaviour. Together, these findings establish a mechanistic contrast between carbon-based and metal-oxide nanomaterials in plant systems, underscoring nanoparticle chemistry as a key determinant of electrochemical response. This comparative framework advances plant nanobionics by linking material composition to bioelectrical function, with implications for bioelectronics, sensing, and sustainable energy interfaces.

Keywords: *Crassula ovata, carbon nanodots (CND), ZnO nanoparticles, impedance spectroscopy, plant nanobionics, biophysics, charge transport.*

1. Introductions

Plants function as dynamic bioelectrical entities, generating and propagating electrical signals that regulate essential physiological processes, including cell division, elongation, nutrient transport, and systemic stress responses[1]. These signals, comprising of action potentials, variation potentials, and system potentials, facilitate rapid intercellular communication and enable plants to adapt to fluctuating environmental conditions[2,3] . The growing recognition of these electrophysiological capabilities has catalysed interest in plants as active components in emerging biohybrid technologies. Plants, with their intrinsic ionic conductivity and organized charge transport pathways, are emerging as sustainable platforms for bioelectronics, energy harvesting, and green storage systems[4] .

Succulent plants have evolved to survive in arid climates by storing water in thick, fleshy tissues, a trait that also imparts distinctive electrochemical properties[5]. In *Aloe vera*, for example, the hydrated pulp can be represented by an equivalent circuit comprising grain and grain boundary impedances, where the grain (chlorenchyma gel) acts as a capacitive energy-storing domain and the grain boundary (parenchyma) governs resistance linked to water retention[6]. Insertion of nanoparticles in plants induce various biophysical changes like enhanced growth, improved photosynthesis, stress tolerance and water retention[7–9] . Excess uptake of NPs, however, has toxic effects such as excessive production of reactive oxygen species, hormonal imbalances and impaired cellular processes[10,11]. These biophysical changes also result in changes in complex impedance of the plant part e.g. Leaves[8,12]. In our earlier communication we showed that the uptake of carbon nanodots (CNDs) in *Aloe vera* decreases energy storage but increases water-retention capacity, highlighting how nanoparticle incorporation modulates charge transport and hydration dynamics[8]. Such findings illustrate how nanomaterials can reshape the intrinsic electrochemical behaviour of succulents, adding a new dimension to their well-known physiological adaptations.

Building on this perspective, *Crassula ovata* (jade plant or lucky plant) provides a particularly attractive model for electrochemical investigations. Native to South Africa and Mozambique and widely cultivated as a hardy ornamental, *C. ovata* combines water-rich tissues with metabolic traits that enable survival under limited moisture[13]. Its leaves and stems function as aqueous electrolyte reservoirs, while mucilage-rich mesophyll and protective pigments support oxidative defence and photoprotection[14]. The CAM metabolism of jade plant further regulates nocturnal CO_2 uptake, stabilizing carbon balance under stress[15]. These features collectively

position *C. ovata* as a reproducible platform for impedance-based studies of plant–nanoparticle interactions. Anatomical adaptations reinforce this potential. Epicuticular waxes restrict transpiration yet allow atmospheric water absorption, while Type I hydathodes facilitate foliar hydration from transient sources such as dew and fog[16]. Combined with amphistomatic leaves and high succulence, these traits establish an internal environment well suited for ionic transport and dielectric response. Nanoparticles entering through the roots are readily translocated via the xylem to aerial tissues, where they accumulate at cell walls, membranes, or vacuoles and influence ion dynamics, membrane potentials, and local conductivity[17,18]. This systemic distribution, supported by uniform transpiration and hydration pathways, creates favourable conditions for interfacial charge storage that can be sensitively probed by electrical impedance spectroscopy.

The convergence of these physiological traits with nanoparticle incorporation aligns with the emerging framework of plant nanobionics, which integrates nanoscale materials into living plants to reconfigure their functional properties[19]. Although nanomaterial uptake has been shown to enhance growth[20], photosynthesis[21], and stress tolerance[22], the electrochemical dimension of plant nanobionics remains underexplored, particularly in succulents. Here, we address this gap by comparing the effects of water-soluble CNDs and ZnO nanoparticles on the electrical behaviour of *C. ovata* using impedance spectroscopy. This comparative approach establishes jade plants as a model system for plant nanobionics and reveals how carbon-based and metal-oxide nanomaterials drive fundamentally different electrochemical responses, governed by progressive pathway obstruction in the case of CNDs and biphasic conduction–polarization dynamics in the case of ZnO.

In this study, we investigate, for the first time, the impact of carbon nanodots (CNDs) and zinc oxide (ZnO NPs) nanoparticles on the electrical behaviour and energy storage mechanism of *Crassula ovata* using impedance spectroscopy. By combining frequency-resolved impedance analysis with equivalent circuit modelling, we quantify how nanoparticle type and concentration govern charge transport, dielectric response, and relaxation dynamics within jade plant tissues. The comparative evaluation of carbon- and metal-oxide-based nanomaterials provides mechanistic insights into ionic mobility, interfacial polarization, and space-charge effects in a living biological matrix. This framework not only elucidates nanoparticle-induced modulation of plant electrochemical properties but also positions *C. ovata* as a reproducible

biological capacitor model, bridging plant physiology with bioelectronic functionality in the emerging field of plant nanobionics.

2. Materials and methods

Materials: Glucose ($C_6H_{12}O_6$), sodium hydroxide pellets (NaOH), anhydrous magnesium sulphate ($MgSO_4$), ethanol, hydrochloric acid (HCl), acetone, and ethylene glycol (EG) were obtained from commercial suppliers and used without further purification. Zinc acetate dihydrate ($Zn(CH_3COO)_2 \cdot 2H_2O$) served as the precursor for ZnO nanoparticle synthesis. Deionized (DI) water was used in all preparations.

2.1 Synthesis of ZnO nanoparticles: Zinc oxide nanoparticles were synthesized using a modified precipitation-solvothermal approach (as shown in Figure.1) in which zinc acetate dihydrate served as the precursor. In a typical preparation, 1.372 g of $Zn(CH_3COO)_2 \cdot 2H_2O$ was dissolved in a 1:1 ethanol-water mixture (125 mL ethanol and 125 mL deionized water) under vigorous stirring to ensure complete dissolution. To this clear solution, 125 mL of freshly prepared 0.10 M NaOH (0.0125 mol) was introduced dropwise while maintaining continuous stirring, which immediately resulted in the formation of a white suspension. The mixture was stirred for several minutes following addition to allow complete precipitation. The solid was separated by centrifugation, washed repeatedly with deionized water until the supernatant reached near neutral pH, and rinsed once with ethanol to remove residual organics. The collected material was subsequently dried at 220 °C for 6 h in an oven to obtain the ZnO precursor.

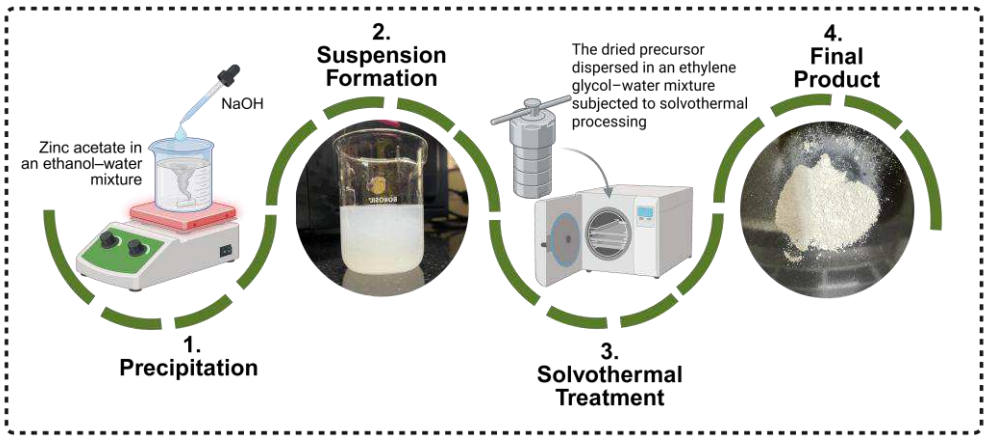

Figure 1. *Schematic illustration of the synthesis of ZnO nanoparticles via a precipitation-solvothermal route. Created with biorender.com*

For the solvothermal step, the dried powder was dispersed in an ethylene glycol-water mixture (50 mL EG and 5 mL water) and preheated to 80 °C with stirring to obtain a homogeneous suspension. This dispersion was transferred into a Teflon-lined stainless-steel autoclave and heated at 200 °C for 6 h. After natural cooling to room temperature, the product was recovered, thoroughly washed with deionized water followed by acetone to remove glycol residues, and finally dried at 80 °C.

2.2 Synthesis of Carbon nanodots: Carbon nanodots were prepared following our previously reported method without modification[8]. In brief, glucose was used as the carbon precursor and subjected to alkaline ultrasonication, followed by pH neutralization, solvent exchange, and lyophilization to yield the CND powder. The complete synthesis protocol and characterization details are described in our previous published work [8].

2.3 Exposure of jade plant to aqueous nanoparticle suspensions*: Crassula ovata* (jade) plants of uniform age and physiological state were sourced from a local nursery in Dehradun, India, to ensure consistency across all experimental groups. A controlled comparative study was carried out to investigate the effects of carbon nanodots (CNDs) and zinc oxide (ZnO) nanoparticles on the electrical and electrochemical behaviour of the plant. Each nanomaterial was applied at three different concentrations - 1 mg/L, 5 mg/L, and 10 mg/L alongside a control group with no nanoparticle treatment as shown in Figure.2. Prior to exposure, the plants were carefully uprooted and thoroughly rinsed with deionized water multiple times to remove all residual soil and surface impurities. This step was essential to prevent any non-specific interactions that could influence nanoparticle uptake. To preserve the integrity of the root structure and ensure optimal nanoparticle absorption, the plants were immersed in nanoparticle suspensions without disturbing their root systems. The cleaned plants were then immersed in 100 mL of their respective nanoparticle suspensions and maintained at room temperature under controlled light conditions for a period of seven days, allowing root-mediated absorption of nanoparticles. Following the exposure period, plants were reintroduced into soil to re-establish root systems under natural growth conditions.

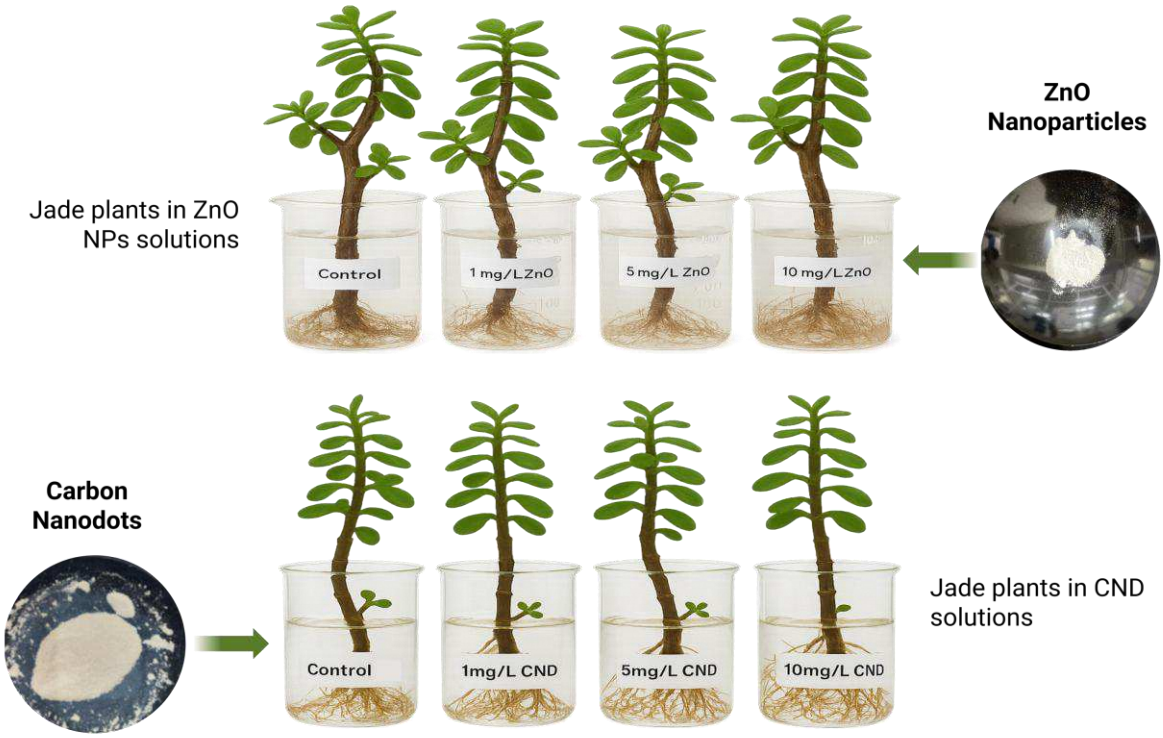

Figure.2 *Schematic showing jade plants treated with varying concentrations of CND and ZnO nanoparticle solutions. Created with biorender.com*

2.4 Characterisation methods*:*

(a) X-ray Diffraction: The crystal structures of the synthesized ZnO and carbon nanodot (CND) powder samples were characterized using X-ray diffraction on a D8 ADVANCE ECO diffractometer (Bruker, Germany) equipped with Cu Kα radiation (λ = 1.5406 Å), operating at 40 kV and 40 mA. The obtained diffraction patterns were further analysed to confirm the phase purity and crystalline characteristics of the materials.

(b) Photoluminescence Spectroscopy: Photoluminescence spectra of the materials were recorded using a PerkinElmer Fluorescence Spectrometer LS 45. For analysis, CNDs were dissolved in water and ZnO nanoparticles were dispersed in ethanol, and the solutions were placed in quartz cuvettes. This setup allowed sensitive detection of emission signals, enabling characterization of the optical properties and electronic transitions of the materials in their respective solvents.

(c) Fourier transform infrared spectroscopy (FTIR) and ATR-FTIR: FTIR analysis (PerkinElmer Frontier; 500-4000 cm^{-1}) was employed to probe the structural signatures of the synthesized nano material and the corresponding treated plant samples. For the ZnO, finely milled powder was blended with spectroscopic-grade KBr and compressed into pellets. Fourier-transform infrared (FTIR) spectra of CNDs were recorded using a Shimadzu IR Affinity-1S WL spectrometer equipped with a diamond ATR and KBr pellet accessory. The system offers a resolution of 0.5 cm^{-1} and enables non-destructive analysis of solid samples, providing high signal stability and sensitivity for identifying functional groups. For analysis, a drop of the aqueous CND solution was directly placed onto the diamond ATR crystal of the Shimadzu IR Affinity-1S WL spectrometer. The evanescent wave generated at the crystal–sample interface enabled direct spectral acquisition without drying or pellet preparation, ensuring accurate detection of surface functional groups in the dispersed state.

(d) AC impedance spectroscopy: Electrical characterization of Aloe vera leaves subjected to nanoparticle treatment was performed using AC impedance spectroscopy (WAYNE KERR 6500B; RRCAT, Indore, India). Fresh leaves were rinsed with deionized water, cut into 1 × 1 cm sections, and mounted within the sample holder. Impedance spectra were acquired to assess frequency-dependent electrical response and extract key charge-transport parameters.

3. Results and discussion:

3.1 X-ray Diffraction (XRD) Analysis:

(a) CND: X-ray diffraction (XRD) analysis was employed to investigate the structural features of the synthesized CNDs. Figure.3(A) displays a broad dominant peak at $2\theta = 19.7°$, indexed to the (002) plane, along with a weaker feature near 42.2° corresponding to the (101) plane, consistent with earlier reports [8]. A pronounced background signal suggests the presence of amorphous components. Notably, the (002) reflection is shifted to a lower Bragg angle relative to graphite (20.2°), indicating an enlarged lattice parameter *c*. Such a shift is commonly attributed to quantum confinement effects and the incorporation of surface functional groups[23]. The increased interlayer spacing is likely associated with oxygenated moieties, including hydroxyl (-OH), carboxyl (-COOH), carbonyl (C=O), and ether (-C-O-), which improve hydrophilicity and promote water dispersibility[24]. The overall amorphous character of the material is reinforced by the breadth of the diffraction peaks, reflecting disruption of extended sp^2 domains. The crystallite size, determined from the (002) reflection using the Scherrer

equation (equation.1), was estimated to be 2.1 ± 0.1 nm after Gaussian fitting and background subtraction. Due to the dominance of amorphous features and the absence of well-defined diffraction peaks, the Williamson-Hall (W-H) analysis was not performed for CNDs, as reliable estimation of microstrain requires distinct, sharp reflections. These results demonstrate that the CNDs possess nanoscale graphitic domains with significant structural disorder, where interlayer expansion and surface functionalization critically influence solubility and electronic properties. The combination of broadened diffraction features and small crystallite size confirms the successful preparation of water-dispersible CNDs suitable for diverse applications.

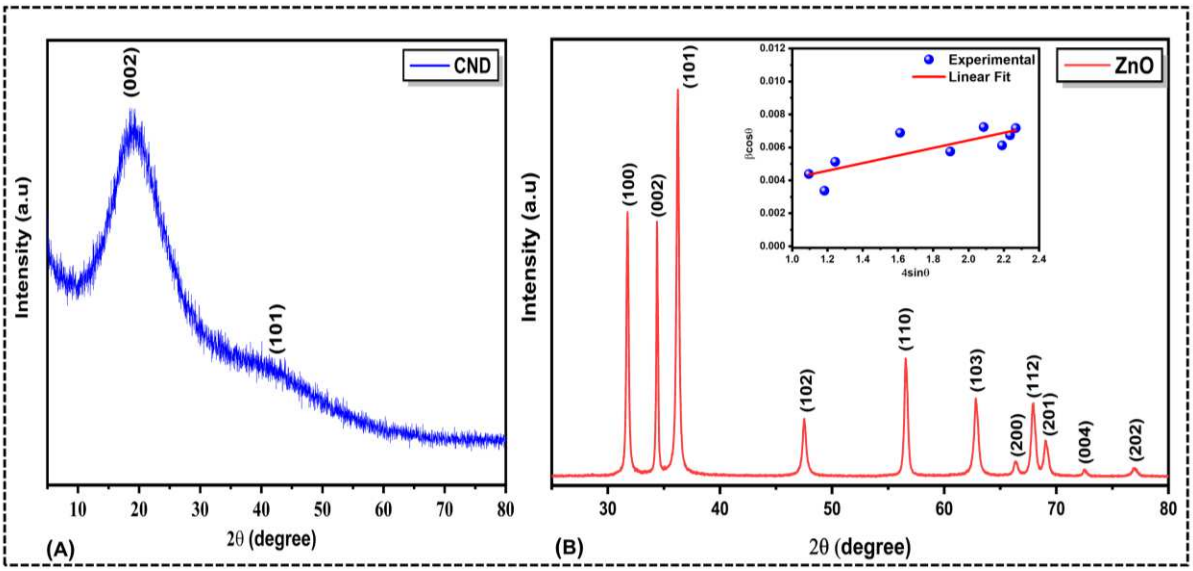

Figure.3. *X-ray diffraction patterns of synthesized nanomaterials. (A) Carbon nanodots (CNDs) displaying a broad diffraction peak at 2θ ≈ 23°, corresponding to the (002) plane of amorphous graphitic carbon. (B) Zinc oxide nanoparticles (ZnO NPs) showing distinct peaks indexed to the hexagonal wurtzite phase, confirming their crystalline nature. The inset shows the Williamson-Hall (W-H) plot of ZnO nanoparticles.*

(b) ZnO Nanoparticles: The crystalline structure of the synthesized ZnO nanomaterials was investigated using X-ray diffraction (XRD) (Figure.3(B)). The diffraction peaks could be indexed to the hexagonal wurtzite structure of ZnO with a space group *P63mc*, which is in excellent agreement with the standard JCPDS card No. 36-1451 [25]. The calculated lattice parameters were $a = b = 3.25$ *Å*, $c = 5.21$ *Å*, $\alpha = \beta = 90°$, and $\gamma = 120°$, confirming the phase purity and hexagonal crystal nature of ZnO.

The average crystallite size (D) was estimated using the Debye-Scherrer equation [26]:

$$D = \frac{K\lambda}{\beta cos\theta} \text{----------(1)}$$

where K is the shape factor (0.9), λ is the wavelength of Cu Kα radiation (1.54 Å), β is the full width at half maximum (FWHM), and θ is the Bragg angle. The crystallite size obtained from the Scherrer equation was further complemented by the Williamson–Hall (W–H) method (Figure.3(B) inset), which is expressed as [26]:

$$(\beta_{total}\cos\theta) = \varepsilon(4\sin\theta) + \frac{K\lambda}{D} \text{----------(2)}$$

Where ε represents the micro strain. From W–H analysis, the average crystallite size was calculated to be ~25.5 nm, which is consistent with the Scherrer estimate. The micro strain was determined to be 0.0023 ± 0.00059. The lattice distortion (δ), calculated using [27]:

$$\text{Dislocation density } (\delta) = \frac{1}{D^2} \text{ ----------(3)}$$

was found to be approximately 1.54×10^{-3} nm^{-2}, indicating the presence of slight lattice imperfections.

These crystallographic parameters are highly relevant for subsequent plant–nanomaterial interaction studies. The crystallite size (~25.5 nm) lies well below the ~50 nm threshold, a range where nanoparticles are reported to penetrate root cell walls and vascular tissues efficiently [25,28,29]. Smaller crystallites provide a higher surface area-to-volume ratio, enhancing Zn^{2+} ion dissolution, which may serve as a micronutrient source but could also induce oxidative stress depending on dosage [28,30]. The observed micro strain (ε) suggests the presence of lattice distortions and defect sites, which typically increase surface reactivity and ion release in the rhizosphere. Similarly, the dislocation density (δ) highlights lattice imperfections that enhance interactions with plant exudates and biomolecules, potentially modulating nanoparticle uptake, aggregation, and bioavailability [31,32]. Together, these findings suggest that the structural features of the synthesized ZnO nanomaterials strongly influence their potential role as both nutrient carriers and stress-inducing agents in plant systems. The summarized role of these crystallographic parameters in plant–nanomaterial interactions is presented in Table 1.

Table 1. *Correlation of ZnO nanomaterial crystallographic parameters (from XRD) with their potential roles in plant uptake and interactions.*

Parameter	Plant Interaction Mechanism	Findings
Crystallite Size (~25 nm)	Enhances uptake and translocation; small size facilitates transport	Smaller NPs ≤50 nm: better uptake/translocation[28]; Leaf uptake limited >60 nm [29,33].
Microstrain and dislocations	Increases surface reactivity, dissolution, and interaction with biomolecules (e.g., root exudates)	Strain/dislocations affect functional behavior [31]; Defects influence NP fate in agroecosystems [32].

3.2 Photoluminescence spectroscopy

The photoluminescence (PL) spectra of carbon nanodots (CNDs) and zinc oxide nanoparticles (ZnO NPs) exhibit distinct emission features that reflect their intrinsic electronic structures and surface states (Figure.4 (A) and Figure.4 (B)). Under UV excitation (365 nm), the CND solution displayed a light green fluorescence, consistent with the broad emission band extending from the blue to green region (~400-520 nm) in the emission spectrum (Figure.4(A)). The prominent emission peak centered around 450 nm, accompanied by a weak shoulder near 480 nm, can be attributed to radiative recombination through surface defect–mediated transitions associated with oxygen-containing functional groups. Similar greenish emission features have been widely reported for carbon nanodots synthesized from biomass-derived precursors or carbohydrate sources, where the surface is enriched with –OH, –COOH, and C=O moieties[34,35]. According to Wang et al[36], such visible-range luminescence originates from edge or defect states formed by carbon atoms at the periphery of the sp^2-hybridized carbon core bonded with carbonyl and carboxyl groups. These localized emissive centers hybridize with π-states of the conjugated carbon backbone, creating radiative traps that facilitate green emission. The dominance of this emission pathway in the present CNDs suggests that the recombination process is primarily governed by surface-state transitions rather than intrinsic π–π* core transitions, consistent with previous reports describing excitation-dependent PL behavior in carbon nanodots[37,38]. The observed fluorescence thus reflects the crucial role of surface functionalization and oxygenated edge defects in dictating the optical response of CNDs, corroborating their defect-state-dominated emission mechanism.

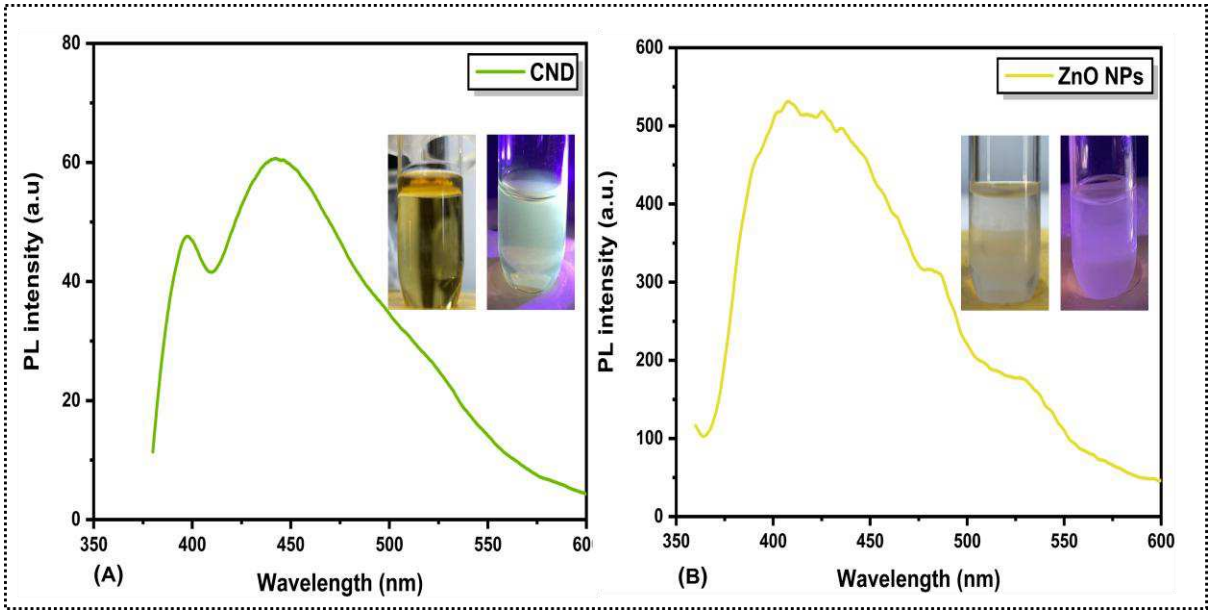

Figure.4 *Photoluminescence spectra of synthesized nanomaterials. (A) Carbon nanodots (CNDs) showing broad emission near 445 nm due to surface defect states. (B) Zinc oxide nanoparticles (ZnO NPs) exhibiting visible emission around 440 nm attributed to intrinsic defects. The spectra confirm the formation of luminescent nanostructures relevant to plant–nanomaterial interaction studies.*

In the case of ZnO NPs, a prominent visible emission band is observed around 440 nm, originating from defect-related transitions such as oxygen vacancies and zinc interstitials. the ZnO nanoparticle dispersion appeared milky white due to light scattering from nanosized particles suspended in the medium. Upon UV excitation (365 nm), the same solution emitted a bluish-white fluorescence, consistent with defect-mediated photoluminescence of ZnO nanostructures. The visible emission arises primarily from deep-level transitions associated with intrinsic point defects, including oxygen vacancies and zinc interstitials, which generate radiative recombination pathways in the blue–green spectral region (~440-500 nm)[39]. Such broad-band visible emission is widely reported for colloidal ZnO nanoparticles and reflects their high density of surface defect states that act as luminescent centres. The observed bluish-white glow therefore indicates the presence of these defect-related radiative transitions within the ZnO lattice[40].

3.3 Fourier transformation infrared spectroscopy (FTIR):

(a) CND: The FTIR spectrum of the carbon nanodots (CNDs) (Figure. 5(A)) reveals multiple vibrational features characteristic of oxygen- and carbon-based surface functionalities. A broad absorption band centred near 3330 cm^{-1} corresponds to the O-H stretching vibration,

confirming the presence of hydroxyl groups that promote water dispersibility and hydrogen bonding[41]. A distinct band around 2978 cm^{-1} arises from the symmetric and asymmetric stretching of aliphatic C–H bonds, indicating residual organic moieties derived from the precursor or surface modification[42]. A weaker feature at 2903 cm^{-1} further supports the presence of aliphatic C–H vibrations, consistent with non-aromatic organic groups decorating the nanodot surface[42]. The sharp and intense absorption at 1639 cm^{-1} is assigned to the C=O stretching vibration of carbonyl groups, likely originating from carboxylic or amide functionalities that influence the emissive behaviour of the CNDs[43]. Additional peaks at 1043 cm^{-1} and a shoulder at 1085 cm^{-1} correspond to C-O stretching modes, indicative of ether linkages contributing to structural stability and fluorescence in aqueous media[42]. These spectral signatures confirm that the synthesized CNDs possess abundant oxygenated surface groups that underpin their solubility and optical performance.

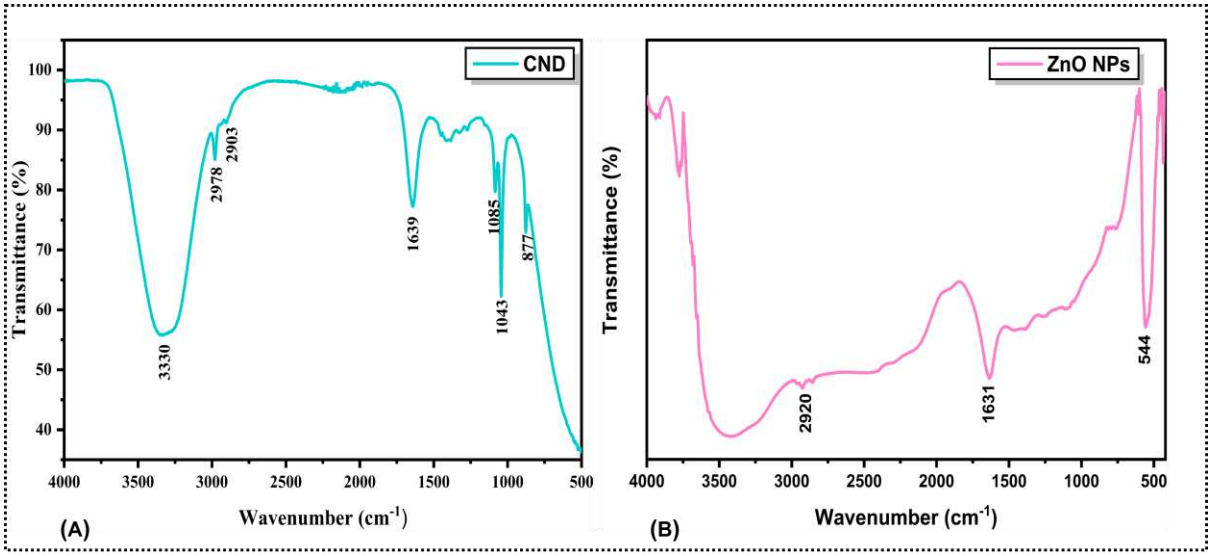

Figure.5 *FTIR spectra of CNDs (A) and ZnO nanoparticles (B). The spectra confirm the presence of characteristic functional groups indicating successful formation and surface functionalization of the nanomaterials.*

(b) ZnO nanoparticle: The FTIR spectrum of the chemically synthesized ZnO nanoparticles displayed characteristic absorption bands corresponding to surface functional groups and Zn-O vibrations (refer Figure.5(B)). A broad band observed at 3300-3500 cm^{-1} is attributed to O-H stretching vibrations, indicating the presence of hydroxyl groups on the nanoparticle surface, likely from adsorbed water molecules [25,44]. These hydroxyl groups enhance the hydrophilicity and dispersion of ZnO nanoparticles in aqueous solutions, facilitating their uptake through plant roots and increasing bioavailability. The peak at 2920 cm^{-1} corresponds to C-H stretching

vibrations, which may arise from trace organic residues from the synthesis process [45,46]. The absorption band at 1631 cm^{-1} is assigned to C=O stretching vibrations, commonly associated with adsorbed carbonate species or surface-bound oxygen functionalities on chemically synthesized ZnO [45,47]. These surface groups contribute to the stabilization of nanoparticles in water and influence their interaction with plant root surfaces, potentially affecting ion transport within plant. Finally, the distinct peak observed below 544 cm^{-1} is attributed to Zn-O stretching vibrations, confirming the formation of crystalline ZnO nanoparticles [25,46]. Overall, the FTIR analysis indicates that the nanoparticles possess surface functional groups that can enhance their dispersibility in water and facilitate root uptake, which is relevant for evaluating their effects on plant impedance at different concentrations (1 mg L^{-1}, 5 mg L^{-1}, 10 mg L^{-1}).

3.4 Complex Impedance Analysis:

The absolute value of the complex impedance Z (|Z|), (where Z = R+jX, R denoting the resistance and X denoting the reactance), was evaluated as a function of frequency for jade plant leaves under varying nanoparticle treatments. The impedance magnitude (|Z|) of jade plant leaves treated with carbon nanodots (CNDs) and zinc oxide nanoparticles (ZnO NPs) via root uptake displayed a strong frequency dependence (Figure.6 (A) and 6(B)). The frequency dependence of the absolute value of |Z| appears similar to that of ceramic samples[48,49]. As seen in Figures. 6 (A) and 6(B), the impedance decreases with increasing frequency. The behaviour is attributed to interplay between the charge carriers and relaxation processes, particularly at the grain boundaries between largely conducting grains of the polycrystalline ceramic samples. For CND treatments (Figure.6(A)), the impedance magnitude |Z| increased monotonically with concentration in the low-frequency regime, reflecting progressive suppression of ionic mobility as nanoparticle loading intensified. At 10 mg L^{-1}, |Z| exceeded 1×10^8 Ω at 20 Hz, indicative of restricted conduction pathways and strong interfacial polarization due to charge accumulation. In contrast, ZnO NPs (Figure.6(B)) displayed a non-monotonic response: |Z| peaked at 5 mg L^{-1}, signifying maximal restriction of charge transfer, but declined at 10 mg L^{-1}, suggesting partial restoration of ionic transport through Zn^{2+}-mediated modulation of membrane permeability and defect-assisted conduction. This shows saturation effect in NP uptake beyond 5mg/L uptake of ZnO_2 NPs and may result in toxic effects.

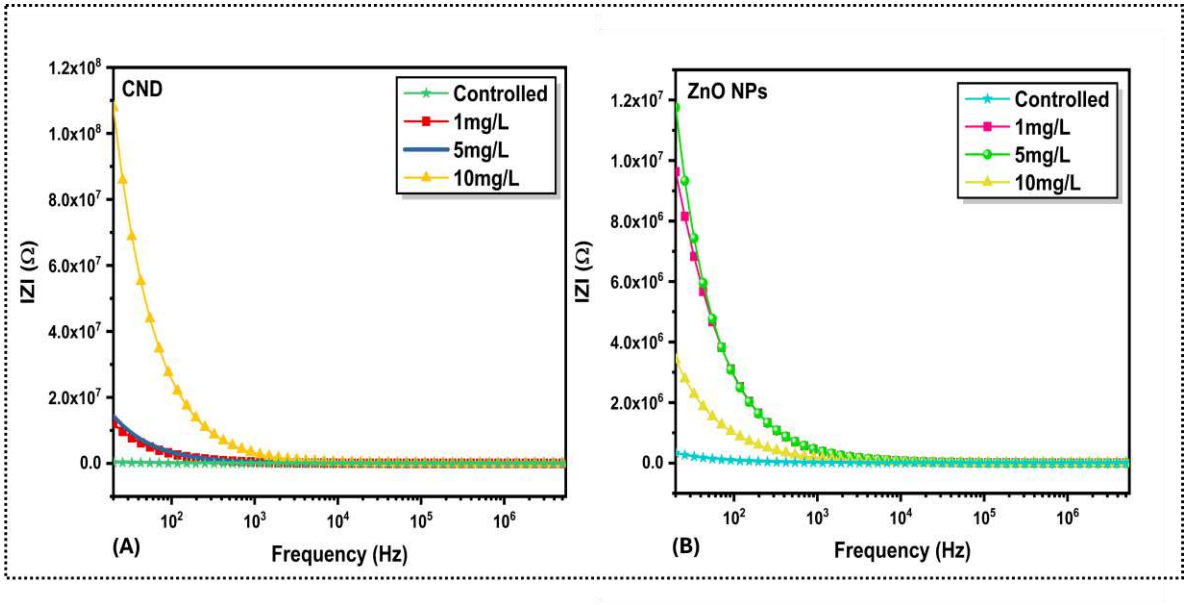

Figure.6 *Frequency-dependent impedance magnitude (|Z|) of Jade plant leaves treated with varying concentrations of (A) carbon nanodots (CNDs) and (B) zinc oxide nanoparticles (ZnO NPs) via root uptake. All treated samples exhibit elevated |Z| in the low-frequency regime (20-10^3 Hz) relative to controls, indicative of enhanced interfacial polarization effects. CNDs show a monotonic |Z| increase with concentration, while ZnO NPs display a non-monotonic trend, with maximum impedance at 5 mg L^{-1} followed by a marked decrease at 10 mg L^{-1}, reflecting distinct nanoparticle-plant tissue interaction mechanisms.*

To study the high frequency electrical behaviour of the Jade plant, negative of the imaginary part vs. real part of the complex impedance (Nyquist plot) for the control leaf sample and the samples spiked with CND and ZnO NPs are plotted in Figure.7(A) and 7(B), respectively. The control sample shows a nearly vertical rise in the middle and the low frequency region. A vertical rise shows the dominance of capacitance in the circuit in this region. At low concentrations, both CND and ZnO uptake exhibit noticeable variations in the Nyquist plot (Figure.7). We have fit a circle to these data and the grain resistances are calculated from the intersection of the circles with the resistance axis.

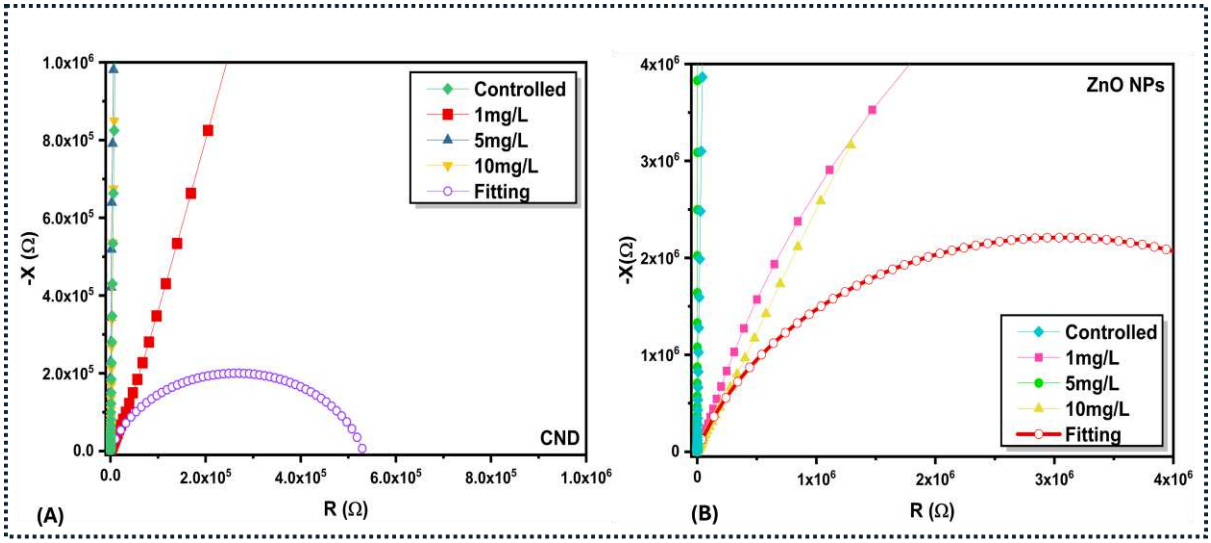

Figure.7 *Nyquist plots of jade plants exposed to carbon nanodots and ZnO nanoparticles. (A) CND treatment shows increased grain boundary resistance with concentration, reflected by elongated arcs indicating restricted ionic transport. (B) ZnO NP exposure yields higher impedance overall, with the largest semicircle at 5 mg L^{-1} and reduced arc at 10 mg L^{-1}, suggesting Zn^{2+}-induced recovery of conduction.*

The grain resistances for 1mg/L uptake of CND and ZnO NPs are 0.6 MΩ and 6.1 MΩ, respectively. The same, calculated for the control sample is found to be of the order of 100 MΩ. For higher CND uptake, the Nyquist plot seems similar to the control sample, with high grain resistance of about 100 MΩ and dominance of capacitance in the equivalent circuit. For ZnO uptake of 5 mg L^{-1}, the leaf shows low grain resistance of 1 MΩ and ~ 100 MΩ for high concentration uptake of 10 mg L^{-1}. The center of the circles fitted for all the samples is in the fourth quadrant, below the real axis. It has been reported that in such cases, the electrical components show non-Debye behaviour, leading to frequency dependence of resistance and ω^{-n} behaviour of capacitance, where n is not equal to 1[50]. For non-Debye behaviour, a constant phase element (CPE) based equivalent circuit model is employed to quantitatively resolve the changes in charge storage and transport properties in jade plant tissues upon nanoparticle uptake. To interpret the impedance spectra, a reduced model comprising two R||C elements in series was adopted (Figure.8), which captures the primary pathways of electrical conduction within the plant matrix. The first parallel branch ($R_1||C_1$) represents the intracellular or grain domain, where R_1 reflects ionic resistance within the cytoplasmic and vacuolar compartments, and C_1 accounts for the pseudo capacitive response arising from ion migration and polarization processes within individual cells. The second branch ($R_2||C_2$) corresponds to the intercellular or grain boundary domain, with R_2 denoting resistance at cell-to-cell junctions and C_2

representing the capacitive contributions from extracellular structures, including plasmodesmata, apoplastic channels, and the polysaccharide rich cell wall network. This simplified framework provides a mechanistic basis for linking nanoparticle induced structural modifications to the observed shifts in the jade plant dielectric and transport behavior.

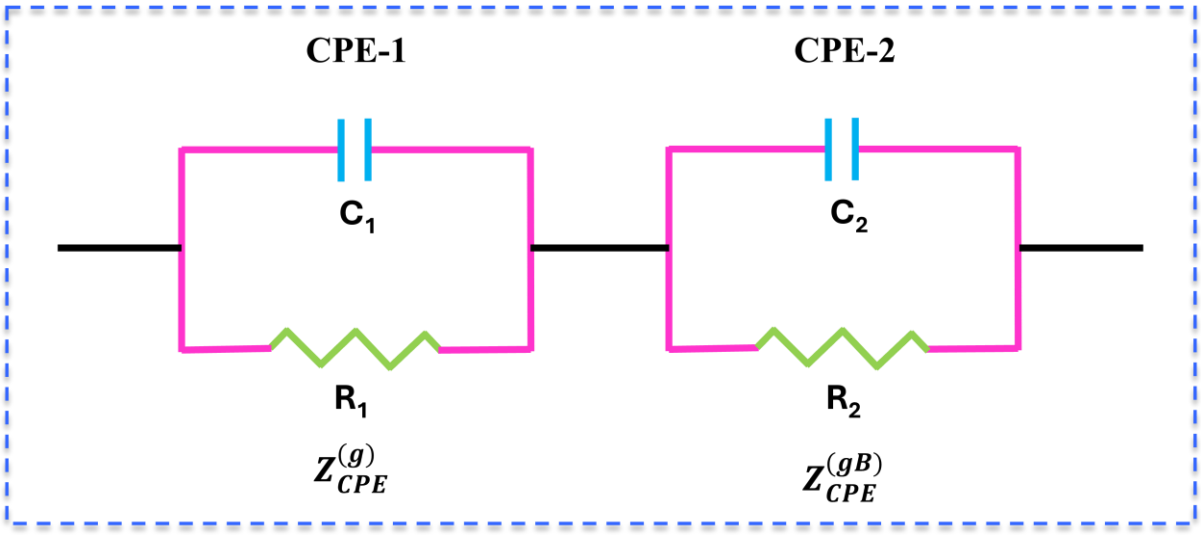

Figure.8 *Simplified equivalent circuit used for impedance analysis of plant tissue, comprising two series-connected R‖C units representing intracellular/grain and extracellular/grain boundary regions to model charge transport and energy storage behavior.*

When the centre of the Nyquist semicircle lies below the real axis, the system exhibits non-ideal Debye-type behavior, indicating deviations from purely resistive or capacitive responses[12]. Under such conditions, conventional elements like resistance and capacitance are replaced by a Constant Phase Element (CPE) to more accurately describe the charge transport characteristics. The impedance of a CPE is expressed as[51]:

$$Z_{CPE} = A_{CPE}^{-1}(j\omega)^{-n}$$

Here, the CPE is defined by two parameters: the frequency-independent pre-exponential factor A_{CPE} and the empirical exponent n, which quantifies the extent of deviation from ideal capacitive behavior[52]. To better understand the parameters governing the CPE behavior, the key elements and their corresponding electrical responses are summarized in Table 2.

Table.2 *Physical Interpretation of parameters derived from Constant Phase element model*

Parameter	Meaning	Expression/ behaviour
A_{CPE}	Frequency-independent constant	-
n	CPE exponent defining deviation from ideal capacitance	0< n<1→ non-ideal capacitor n = 1 → ideal capacitor n = 0 → pure resistor
Z_θ	Impedance	$Z_\theta = 1/A_{CPE}$ (n = 0, resistive)[53] $Z_\theta = 1/ A_{CPE}.\omega$ (n = 1, capacitive)[54]

For the jade plant system, the total impedance can be expressed as the sum of contributions from grains and grain boundaries[55]:

$$Z_{CPE} = Z_{CPE}^{(g)} + Z_{CPE}^{(gB)}$$

The grain contribution is defined as:

$$Z_{CPE}^{g} = (A_{CPE}^{g})^{-1}.\omega^{-n_1}.j^{-n_1} \quad \text{.....(4)}$$

$$|Z|_{CPE}^{g} = (A_{CPE}^{g})^{-1}.\omega^{-n_1} \quad \text{.....(4.a)}$$

Similarly for the grain boundary,

$$Z_{CPE}^{gB} = (A_{CPE}^{gB})^{-1}.\omega^{-n_1}.j^{-n_1}$$

$$|Z|_{CPE}^{gB} = (A_{CPE}^{gB})^{-1}.\omega^{-n_1} \quad \text{..... (4.b)}$$

To examine the frequency-dependent electrical behavior of jade plants treated with carbon nanodots (CND) and ZnO nanoparticles, Log-Log plots of |Z| versus frequency were analysed over a wide frequency range (see Figure.9). The resulting graphs reveal three distinct regions. Region I (low frequency) reflects impedance contributions from the electrode-sample interface and contact resistance, dominated by interfacial polarization and ion accumulation. Region II (intermediate frequency) corresponds to grain boundary effects, capturing the resistive-capacitive interplay at intercellular junctions and apoplastic pathways. Region III (high frequency) represents the intrinsic grain or intracellular response, where impedance is largely governed by ionic transport within the cytoplasm and vacuolar compartments.

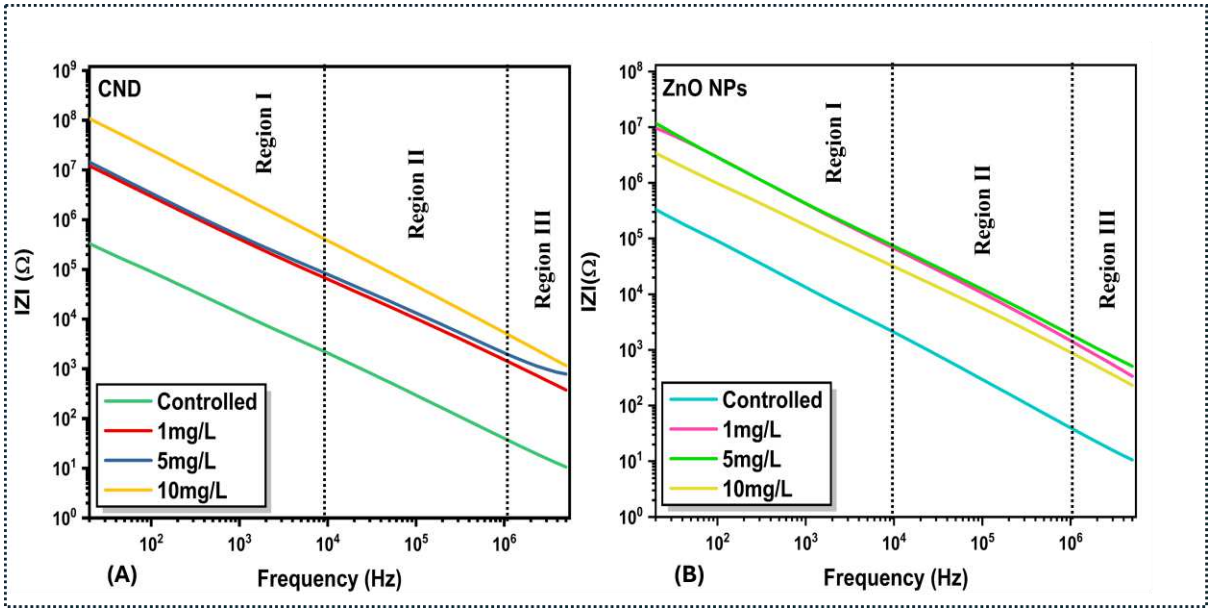

Figure.9 *Impedance spectra of jade leaves treated with (A) carbon nanodots (CNDs) and (B) ZnO nanoparticles (NPs). Log-log plots of |Z| versus frequency highlight three regions: interfacial polarization at low frequency (Region I), resistive–capacitive interplay across cell junctions at intermediate frequency (Region II), and bulk ionic conduction at high frequency (Region III). CNDs induce a monotonic rise in |Z| with concentration, while ZnO NPs display a non-monotonic trend, with maximal impedance at 5 mg L^{-1} and partial recovery at 10 mg L^{-1}, reflecting distinct dose-dependent interactions with plant tissues.*

In Region I (low frequency), both nanomaterial treatments induce a pronounced elevation in |Z| relative to the control, reflecting enhanced interfacial polarization and restricted ionic mobility at the electrode–tissue interface. For CNDs, impedance increases monotonically with concentration, indicating progressively hindered charge transport pathways as nanoparticle loading intensifies (Figure.9(A)). By contrast, ZnO NPs display a non-linear response: the 5 mg L^{-1} treatment yields the highest impedance, whereas the 10 mg L^{-1} treatment nearly converges with the control (refer Figure.9(B)). This reversal suggests that moderate ZnO NP exposure impedes ion movement, but higher doses may promote Zn^{2+}-induced alterations in membrane permeability that partially restore ionic conduction. Such a non-monotonic response is particularly noteworthy, as it implies dose-dependent physiological compensation in plant tissues under ZnO NP stress.

Region II (intermediate frequency) represents a transition domain where resistive and capacitive contributions coexist, arising from charge transport across intercellular junctions and the cytoplasmic matrix. Here, the clear separation observed at low frequency diminishes. For CNDs, the 5 mg L^{-1} and 10 mg L^{-1} treatments display nearly overlapping profiles,

suggesting a saturation threshold beyond which further nanoparticle loading exerts limited influence on tissue conductivity. Similarly, ZnO NP-treated leaves exhibit reduced divergence between concentrations, indicating attenuation of nanoparticle-driven polarization effects as bulk conduction mechanisms become dominant. This transition underscores how nanoparticle-induced perturbations at the membrane interface gradually yield to intracellular charge dynamics with increasing frequency. Region III (high frequency) is characterized by convergence of |Z| across all treatments, signifying that bulk ionic conduction within the cytoplasm and vacuolar compartments dominates while interfacial polarization becomes negligible. Dielectric relaxation in this regime is governed by intrinsic tissue properties, independent of nanoparticle concentration or type.

The data reveal two biologically relevant features: first, the monotonic rise in impedance with CND concentration indicates consistent suppression of ionic mobility, implying direct obstruction of conduction pathways. Second, ZnO NPs show a unique non-monotonic pattern, where moderate exposure strongly restricts charge transfer, but higher exposure partially reverses this effect, likely through Zn^{2+}-mediated modulation of membrane permeability. This adaptive or compensatory response to ZnO NPs, absent in CND treatments, suggests that plants engage distinct physiological mechanisms when interacting with different nanomaterials. To capture the complex dielectric behavior of jade leaves treated with carbon nanodots and ZnO nanoparticles, the impedance spectra were fitted using constant phase elements (CPEs). The use of CPEs is essential in biological systems, where membrane heterogeneity, ionic gradients, and structural disorder lead to clear deviations from ideal capacitive behavior[56]. The impedance of a CPE is expressed as:

$$Z_{CPE} = \frac{1}{A_{CPE}} . \frac{1}{(j\omega)^n} = \frac{1}{A_{CPE}.\omega^n}\left(cos\frac{\pi n}{2} - jsin\frac{\pi n}{2}\right)$$

where A is the pre-exponential factor, n is the dispersion exponent, and ω is the angular frequency. From this representation, the resistive and capacitive contributions can be separated as:

$$R_{CPE} = \frac{1}{A_{CPE}.\omega^n} cos\frac{\pi n}{2}\,,\; C_{CPE} = \frac{A_{CPE}.\omega^{n-1}}{sin\frac{\pi n}{2}}$$

To further dissect the impedance response of jade leaves, the experimental spectra were fitted with equivalent circuits incorporating constant phase elements (CPEs), enabling separation of grain (g) and grain boundary (gB) contributions. The extracted parameters, including the pre-exponential factor (A), dispersion exponent (n), pseudo-capacitance (C_{CPE}), and effective

resistance (R_{CPE}), are presented in Tables 3 and Table 4 for CND and ZnO treated plant samples, respectively. These values provide a quantitative framework for linking nanoparticle dosage with charge storage, polarization, and ionic transport pathways within the plant tissue.

Table.3 *Grain and grain boundary resistance, CPE equivalent circuit parameters for jade plant treated with CND*

Sample	(g) A_{CPE}	n_1	(gB) A_{CPE}	n_2	(g) C_{CPE} (Farad)	(gB) C_{CPE} (Farad)	(g) R_{CPE} Ω	(gB) R_{CPE} Ω
Control	6.31×10^{-8}	0.82	3.50×10^{-8}	0.86	3.3×10^{-9}	6.9×10^{-9}	5.55	256.32
1mg/L	8.13×10^{-10}	0.87	2.06×10^{-9}	0.80	9.6×10^{-11}	2.07×10^{-10}	138.5	12500
5mg/L	3.86×10^{-8}	0.60	1.99×10^{-9}	0.79	1.47×10^{-10}	1.78×10^{-12}	663	16276
10mg/L	6.03×10^{-11}	0.95	9.25×10^{-11}	0.92	1.78×10^{-12}	3.63×10^{-11}	2395.2	27578

For CND-treated leaves, a clear concentration-dependent modulation of electrochemical behavior is observed. At low concentration (1 mg L^{-1}), R_{CPE} at the grain boundary rises sharply to ~12.5 kΩ compared with 256 Ω in the control, accompanied by reduced capacitance, suggesting severe restriction of ion transport across cell junctions. Increasing the dose to 5 mg L^{-1} further elevates both grain and grain boundary resistances (663 Ω and 16.3 kΩ, respectively), while simultaneously reducing the n-values to ~0.60 in the grain region, reflecting a deviation from ideal capacitive behavior. At the highest concentration (10 mg L^{-1}), R_{CPE} values escalate dramatically (2.4 kΩ in the grain and 27.6 kΩ in the grain boundary), with pseudo-capacitance dropping by nearly an order of magnitude. Together, these changes reveal that CND exposure progressively disrupts ionic pathways, enhances polarization, and drives the system toward increasingly resistive and non-ideal capacitive behavior.

In contrast, ZnO NP treatments reveal a non-monotonic trend consistent with the impedance spectra. At 1 mg L^{-1}, grain boundary resistance peaks at ~11 kΩ, more than forty-fold higher than the control, while capacitance values fall, reflecting restricted intercellular transport. However, further increases in concentration do not intensify this resistive effect. At 5 mg L^{-1}, R_{CPE} remains high (~14.6 kΩ), but at 10 mg L^{-1} a pronounced decline is observed, with grain boundary resistance reduced to ~7.3 kΩ and capacitance values partially restored. This reversal, accompanied by stable n-values near 0.8-0.9, suggests that higher ZnO exposure alters membrane permeability, likely through Zn^{2+} interactions, thereby counteracting the polarization-driven resistance observed at moderate concentrations.

Table.4 Grain and grain boundary resistance, CPE equivalent circuit parameters for jade plant treated with ZnO								
Sample	**(g) A_{CPE}**	**n_1**	**(gB) A_{CPE}**	**n_2**	**(g) C_{CPE} (Farad)**	**(gB) C_{CPE} (Farad)**	**(g) R_{CPE} Ω**	**(gB) R_{CPE} Ω**
Control	6.48×10^{-8}	0.82	3.50×10^{-8}	0.86	3.37×10^{-9}	3.5×10^{-9}	5.45	255.98
1mg/L	4.17×10^{-10}	0.91	1.41×10^{-9}	0.83	6.66×10^{-10}	2×10^{-10}	96.8	10991.6
5mg/L	1.63×10^{-9}	0.81	2.1×10^{-9}	0.79	7.18×10^{-11}	1.88×10^{-10}	275.4	14586.7
10mg/L	1.96×10^{-9}	0.84	6.7×10^{-9}	0.77	1.429×10^{-10}	4.25×10^{-10}	115	7325.3

These findings highlight two distinct modes of nanoparticle interaction with plant tissues. CNDs exert a progressive, concentration-dependent suppression of ionic mobility, consistent with direct obstruction of conduction pathways. On the other hand, ZnO NPs display a dose-sensitive biphasic effect, where moderate exposure strongly restricts charge transport, but higher concentrations trigger physiological or structural adaptations that partially restore conductivity. This divergence underscores that nanoparticle chemistry and dosage determine not only the extent but also the direction of electrochemical modulation in plant tissues, offering mechanistic insight into how nanomaterials perturb ionic homeostasis at the cellular and intercellular level.

3.5 Frequency-Dependent Dielectric Response

The dielectric response and AC conductivity provide intrinsic information about the electrical behavior of Jade plant, independent of its macroscopic geometry. Unlike resistance (R) and reactance (X), which vary with sample size, dielectric parameters are governed by polarization dynamics and charge transport within the cellular matrix[57]. The complex permittivity ($\varepsilon^* = \varepsilon' + i\,\varepsilon''$) describes energy storage (ε') and dissipation (ε'') under an alternating field, and can be obtained from impedance spectra using:

$$\varepsilon' = \frac{X}{|Z|^2 \omega C_o}, \quad \varepsilon'' = \frac{R}{|Z|^2 \omega C_o}$$

where |Z| is the impedance magnitude, ω is the angular frequency, and $C_o = \varepsilon_o a/d$ the vacuum capacitance of a parallel-plate configuration with electrode area a, tissue thickness d, and free-space permittivity ε_o. Normalization by C_o ensures that the derived dielectric parameters reflect the intrinsic polarization and charge transport properties of *Jade* leaves, thereby enabling direct assessment of nanoparticle-induced modifications in tissue electrochemical behavior.

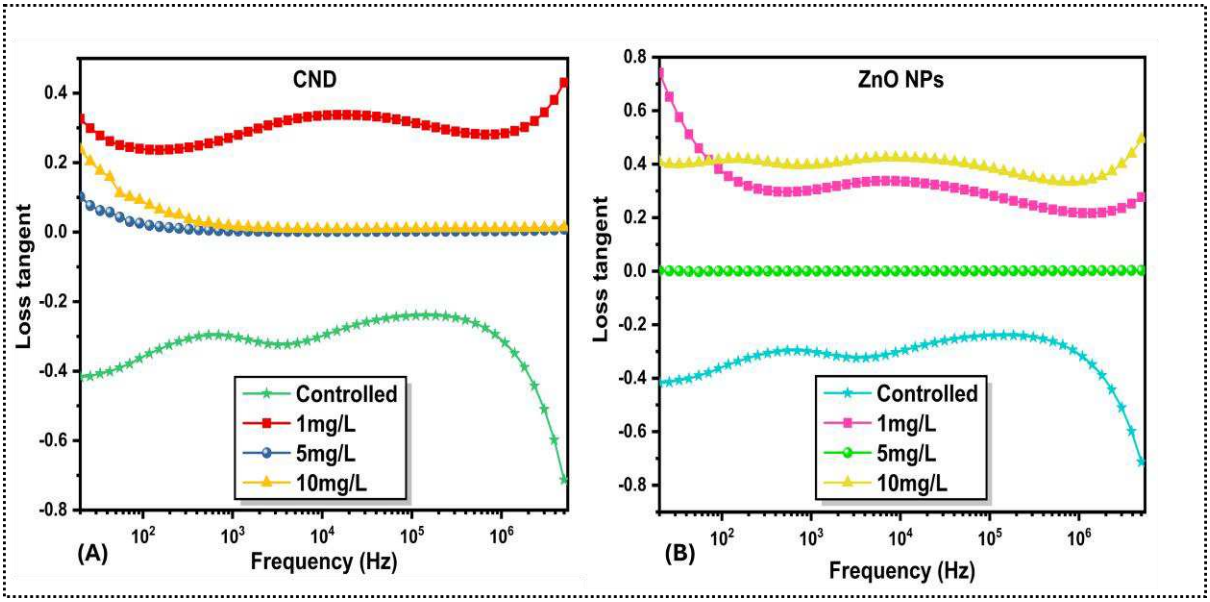

Figure.10 *Frequency-dependent loss tangent of jade plants treated with CNDs and ZnO nanoparticles. (A) CND treatment shows elevated tan δ at 1 mg L^{-1} due to enhanced dipolar relaxation, followed by suppression at higher concentrations from charge blocking. (B) ZnO NPs exhibit a biphasic trend, with relaxation enhancement at 1 mg L^{-1}, suppression at 5 mg L^{-1}, and recovery at 10 mg L^{-1} from defect-mediated conduction.*

The loss tangent (tan δ) profile as a function of frequency, Figure.10(A) and 10(B) revealed notable differences between CND- and ZnO-treated plants, respectively compared to the control. The tan δ spectra revealed that at low CND concentration (1 mg L^{-1}), dielectric losses increased, consistent with enhanced dipolar relaxation. However, higher doses (5-10 mg L^{-1}) suppressed tan δ, reflecting reduced leakage and a more ideal capacitor-like response. This trend aligns with ε′ analysis, which showed that CNDs decreased absolute permittivity across all concentrations, indicating reduced polarization capacity due to nanoparticle blocking. Together, these results imply that while CNDs diminish charge storage ability, they also lower dielectric losses, effectively shifting tissues toward more resistive yet efficient capacitor-like behavior.

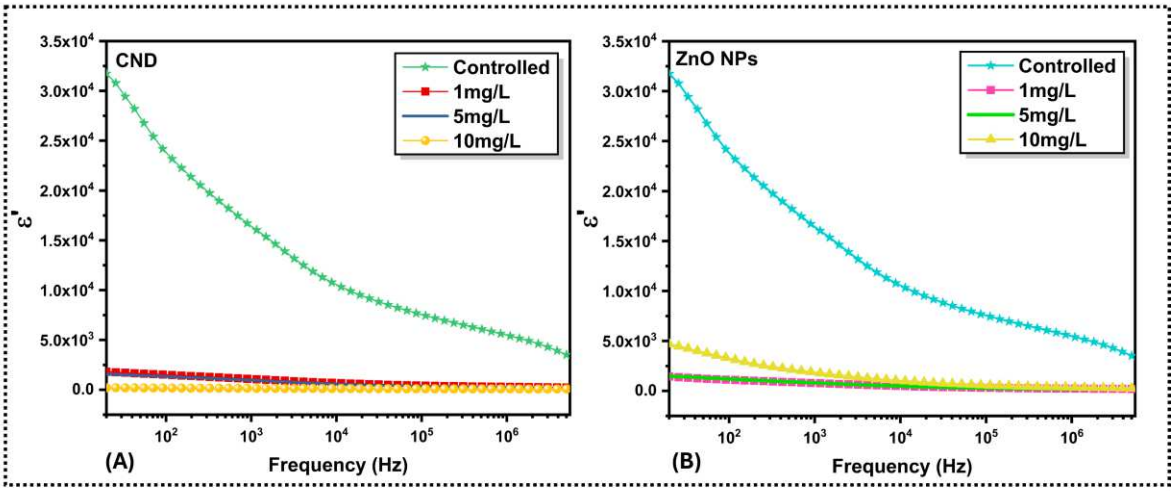

Figure.11 *Dielectric permittivity (ε′) of jade plants treated with CNDs and ZnO nanoparticles. Controls show high ε′ at low frequencies, decaying with frequency due to interfacial polarization. CNDs (A) suppress ε′ across all concentrations, reflecting reduced polarization capacity from nanoparticle blocking. ZnO NPs (B) exhibit a biphasic trend: low concentration reduces ε′, while higher doses (5-10 mg L^{-1}) partially restore permittivity via defect-assisted polarization.*

In parallel, the dielectric constant (ε′) exhibited a strong frequency dependence as shown in Figure 11(A) and 11(B) for CND and ZnO, respectively. At lower frequencies, ε′ values were markedly higher, driven by space charge and interfacial polarization effects, which dominate when ions accumulate at cell walls and membranes. With increasing frequency, ε′ steadily decreased across all treatments, reflecting the inability of dipoles and charges to follow the rapidly alternating field. The reduction in ε′ was more pronounced for ZnO-treated plants, whereas CND treatments preserved higher dielectric permittivity at intermediate frequencies, suggesting differences in how these nanomaterials interact with cellular structures. Importantly, the coupled analysis of tan δ and ε′ indicates that nanoparticles not only alter the efficiency of charge storage but also modulate dielectric losses, thereby influencing the balance between capacitive energy storage and dissipative processes within plant tissues.

3.6 Frequency dependent AC conductivity

In succulents such as jade plant (*Crassula ovata*), the frequency-dependent response reflects the combined effects of ionic migration through the hydrated matrix and polarization at cell wall–membrane interfaces. When leaves are treated with carbon nanodots (CNDs) or ZnO nanoparticles, changes in the conductivity spectra indicate modifications in both long-range and localized transport pathways.

The overall conductivity can be derived from impedance parameters as:

$$\sigma_T = \frac{\varepsilon_o R}{C_o IZI^2}$$

where ε_0 is the permittivity of free space, R is the real impedance, C_0 is the geometric capacitance, and |Z| is the modulus of impedance. This conductivity can be separated into a static contribution (σ_{dc}), associated with extended ion migration, and a frequency-dispersive term σ(ω) linked to hopping events:

$$\sigma_T = \sigma_{ac}(\omega) = \sigma_{dc} + \sigma(\omega)$$

The dispersive behavior is often captured using Jonscher's universal power law:

$$\sigma_{ac}(\omega) = \sigma_{dc} + A\omega^s$$

where A is a constant and s is the frequency exponent. The value of s provides mechanistic insights, with $0 < s < 1$ pointing to translational hopping in disordered matrices, while $s > 1$ suggests localized or orientational hopping processes. In the conductivity spectra (Figure 12(A) and 12(B) for CND and ZnO, respectively), both CND- and ZnO-treated leaves show the characteristic rise in σac with frequency, reflecting the increasing contribution of short-range hopping at higher frequencies. At lower frequencies, σac tends to plateau, corresponding to the dominance of dc conduction associated with long-range ion migration through tissue fluids.

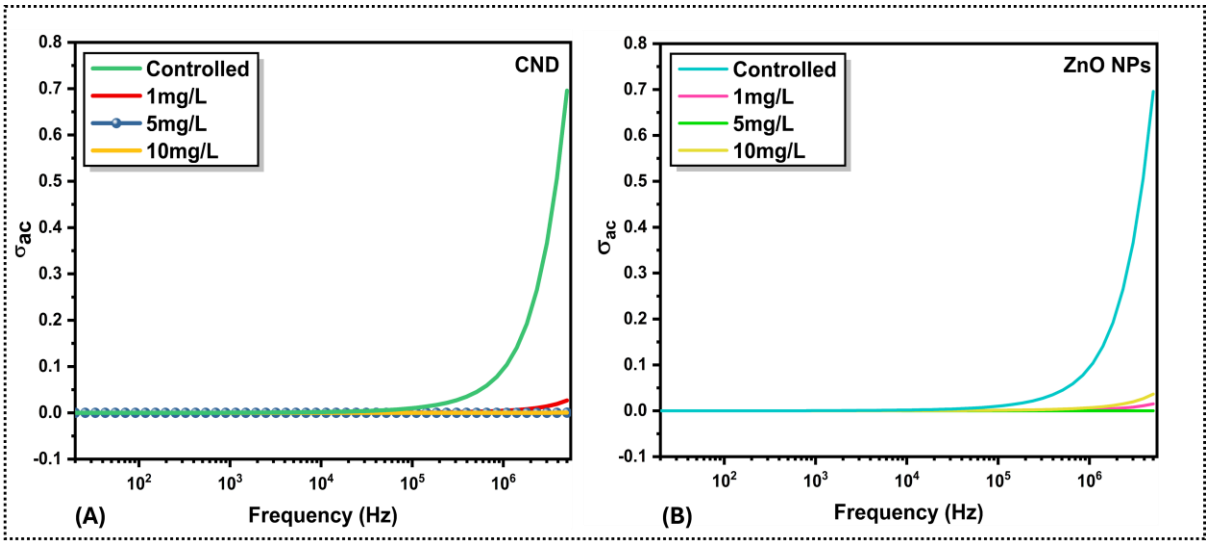

Figure.12 *Frequency-dependent AC conductivity of jade plant leaves treated with nanoparticles. Variation of σac with frequency for Crassula ovata leaves exposed to carbon nanodots (CNDs) (A) and ZnO nanoparticles (B). Both treatments modify the balance*

between dc conduction and frequency-dispersive transport, with CNDs promoting gradual hopping-mediated conductivity and ZnO inducing stronger interfacial polarization effects.

The frequency-dependent features of AC conductivity in jade leaves exposed to CNDs and ZnO nanoparticles were further examined using $\log(\sigma_{ac}(\omega) - \sigma_{dc})$ versus log(frequency) representations (Figure.13(A) to 13(D); Figure.14(A) to 14(D). These plots consistently delineate three conduction regimes. At low frequencies, conductivity remains nearly constant, reflecting electrode–tissue interfacial polarization. The intermediate domain, identified as region X, corresponds to intercellular or grain boundary conduction, whereas the high-frequency region Y represents charge transport within intracellular or grain domains. Linear fits applied to regions X and Y allowed the determination of Jonscher's parameters *s* and *A*, which characterize the power-law dependence of AC conductivity. Comparative analysis revealed that CND treatment promotes a smoother progression from region X to Y, consistent with enhanced translational hopping across the disordered cellular framework.

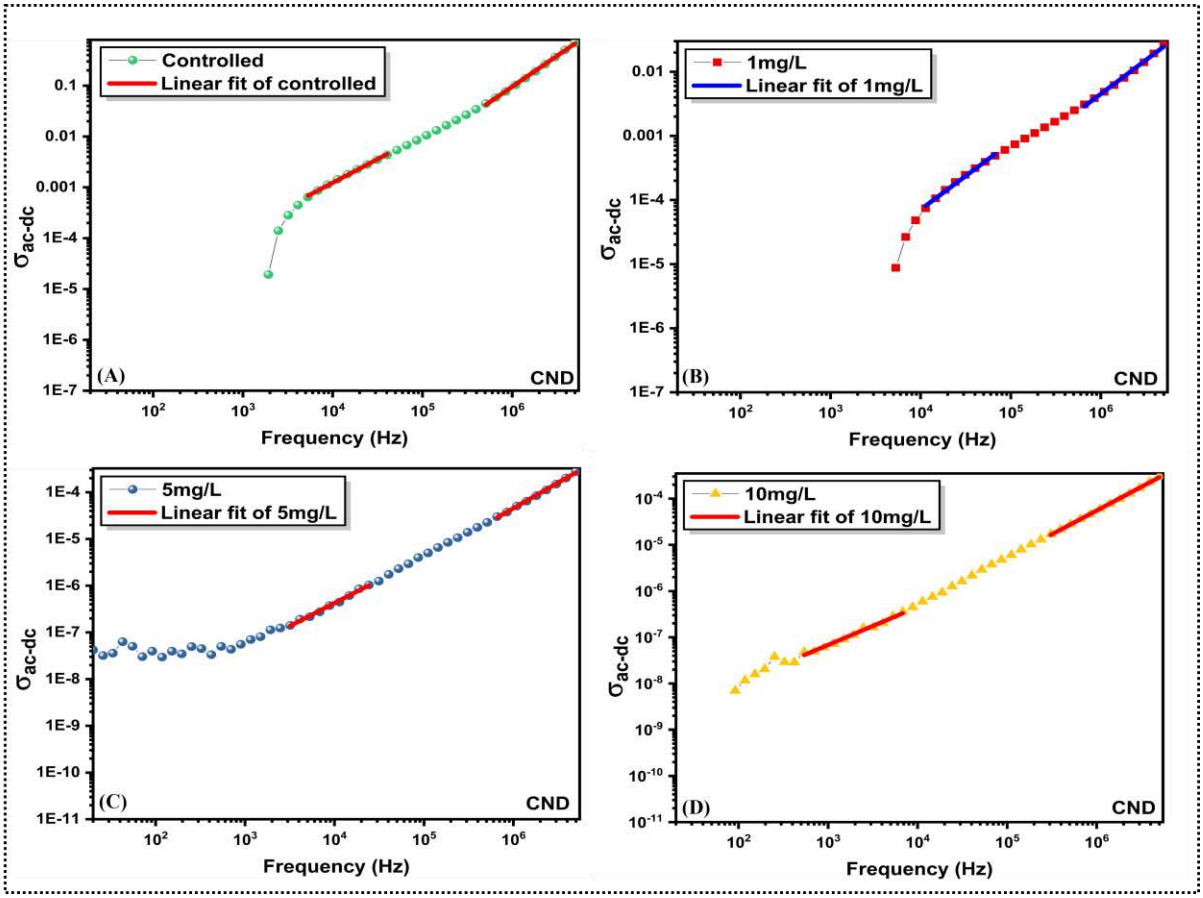

Figure.13 *Log-log plots of AC conductivity in jade plant leaves treated with CNDs. Log-log plots of ($\sigma_{ac} - \sigma_{dc}$) versus frequency for (a) control, (b) 1 mg L^{-1}, (c) 5 mg L^{-1}, and (d) 10 mg L^{-1} treatments. Three conduction regions are evident: low-frequency interfacial effects, intermediate region X (intercellular/grain boundary transport), and high-frequency region Y (intracellular/grain conduction). Linear fits to regions X and Y provided Jonscher's parameters s and A, showing smoother transitions and enhanced hopping transport under CND exposure.*

In contrast, ZnO-treated samples show a sharper rise in the high-frequency domain, consistent with localized polarization and charge trapping at cellular interfaces. Together, these results highlight how distinct nanomaterials modulate hopping dynamics in jade tissues by differentially tuning intercellular and intracellular conduction regimes.

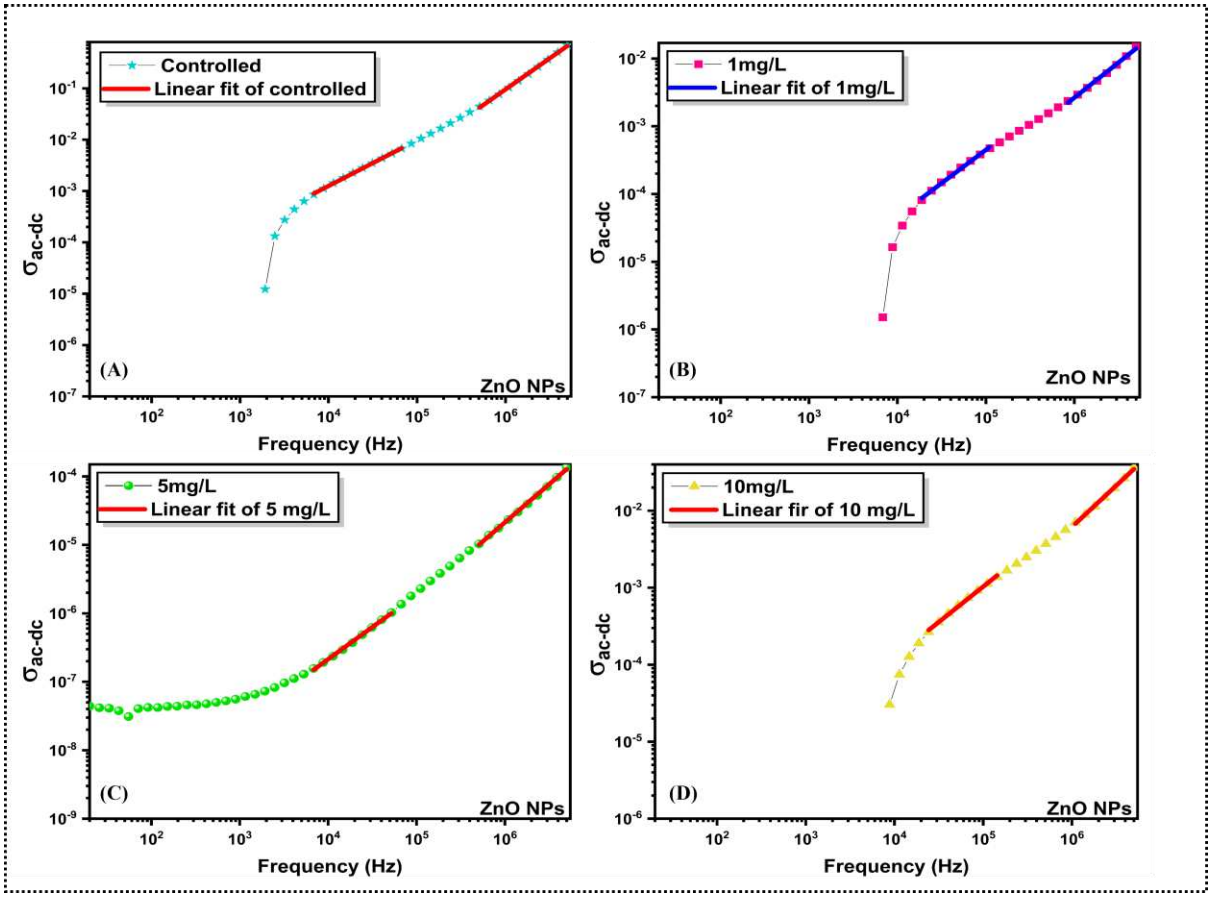

Figure.14 *Log-log plots of AC conductivity in jade plant leaves treated with ZnO nanoparticles. Log–log plots of ($\sigma_{ac} - \sigma_{dc}$) versus frequency for (a) control, (b) 1 mg L^{-1}, (c) 5 mg L^{-1}, and (d) 10 mg L^{-1} treatments. The spectra display the same three conduction regions as in CND-treated samples, but ZnO exposure results in a steeper slope in region Y, reflecting localized polarization and charge trapping. Fitted Jonscher's parameters confirm the distinct conduction behavior induced by ZnO nanoparticles.*

The Jonscher parameters extracted from conductivity spectra highlight distinct responses of jade plant tissues to CND and ZnO treatments are listed in Table.5 and Table.6 respectively. In plants exposed to CNDs, the grain exponent (s_1) shows a pronounced concentration-dependent shift. At 1 mg L^{-1}, s_1 increases to 1.05 from the control value of 0.93, reflecting enhanced long-range hopping within the grains, but declines to 0.82 at 10 mg L^{-1}, indicative of disrupted conduction pathways under higher loading. The pre-exponential factor (A_1) mirrors this trend, with values reduced by several orders of magnitude at 5 mg L^{-1} (4.8×10^{-11}), pointing to effective passivation of defect-mediated hopping at intermediate concentrations. Grain boundary conduction also exhibits suppression, with s_2 decreasing from 1.21 in the control to ~1.0 -1.05 in treated samples, and A_2 reaching its minimum at 5 mg L^{-1} (1.25×10^{-11}), consistent with diminished interfacial polarization. At the highest CND concentration (10 mg L^{-1}), the conduction response deviates sharply from the trends observed at lower doses. The grain

exponent (s_1) falls to 0.82, reflecting a shift from extended hopping to more localized transport. This behaviour likely arises from nanoparticle overloading, where agglomeration within cytoplasmic domains disrupts percolation pathways and introduces additional scattering centres. Such excess loading may also interfere with membrane-associated transport processes, effectively suppressing long-range conduction.

Table.5 *Jonscher's parameters for AC conduction in grain and grain boundary for jade plant treated with CND*

Sample	Grain conduction			Grain boundary conduction		
	s_1	A_1	R^2	s_2	A_2	R^2
Control	0.928	2.4×10^{-7}	0.997	1.21	5.12×10^{-9}	0.999
1mg/L	1.05	4.6×10^{-9}	0.993	1.05	2.04×10^{-9}	0.995
5mg/L	0.985	4.8×10^{-11}	0.998	1.09	1.25×10^{-11}	0.993
10mg/L	0.82	2.36×10^{-10}	0.986	1.03	3.75×10^{-11}	0.999

ZnO treatment, in contrast, induces more gradual changes. In the grain region, s_1 rises modestly from 0.89 to 0.98 at 1 mg L^{-1} and stabilizes around 0.92 at 10 mg L^{-1}, suggesting a subtler modulation of grain conduction. The associated A_1 values also decrease at 5 mg L^{-1} (3.8×10^{-11}) but without the abrupt suppression characteristic of CNDs. Grain boundary conduction is more strongly affected by ZnO: s_2 decreases from 1.20 in the control to ~1.04-1.07 upon treatment, while A_2 reaches an exceptionally low value at 5 mg/L (4.57×10^{-12}), almost an order of magnitude lower than the corresponding CND treatment, underscoring a stronger attenuation of boundary-mediated transport.

At the highest nanoparticle concentration (10 mg L^{-1}), both treatments depart from the trends observed at lower doses, but in distinct ways. For CNDs, the grain exponent (s_1) drops sharply to 0.82, indicating a transition from extended hopping to more localized conduction. This decline likely reflects overloading effects, where excess CNDs agglomerate within cytoplasmic domains, disrupt percolation pathways, and introduce scattering centres that suppress long-range transport. In contrast, ZnO shows a more stable response at 10 mg L^{-1}, with s_1 settling near 0.92 and boundary parameters (s_2, A_2) displaying only modest changes.

Table.6 *Jonscher's parameters for AC conduction in grain and grain boundary for jade plant treated with ZnO*						
Sample	**Grain conduction**			**Grain boundary conduction**		
	s_1	**A_1**	**R^2**	**s_2**	**A_2**	**R^2**
Control	0.89	3.41×10^{-7}	0.999	1.2	5.12×10^{-9}	0.999
1mg/L	0.98	5.5×10^{-9}	0.994	1.04	1.5×10^{-9}	0.995
5mg/L	0.94	3.8×10^{-11}	0.998	1.1	4.57×10^{-12}	0.998
10mg/L	0.92	3.16×10^{-8}	0.996	1.07	2.18×10^{-9}	0.997

These results reveal a clear divergence in conduction pathways influenced by the two nanomaterials. CNDs predominantly modulate conduction within the grain interiors, producing a sharp concentration-dependent transition from enhanced to suppressed transport, while ZnO exerts its strongest effects at the grain boundaries, where interfacial polarization is selectively suppressed.

3.8 Electric modulus:

The electric modulus provides a reliable framework for probing relaxation dynamics in plant tissues. By presenting the dielectric response in terms of modulus, the influence of electrode polarization is largely suppressed, allowing bulk processes to be more clearly resolved. The complex modulus (M^*) is defined as the reciprocal of complex permittivity (ε^*):

$$M^* = \frac{1}{\varepsilon^*} = M' + jM''$$

where M' and M'' denote the real and imaginary components, respectively. These are related to the dielectric constant (ε') and dielectric loss (ε'') according to:

$$M' = \frac{\varepsilon'}{\varepsilon' + \varepsilon''} \quad \text{and} \quad M'' = \frac{\varepsilon''}{\varepsilon' + \varepsilon''}$$

The electric modulus spectra of jade plants treated with CNDs and ZnO NPs reveal distinct nanoparticle-dependent relaxation dynamics (Figure). For CNDs, M′ increases monotonically with frequency across all concentrations, with the strongest response observed at 10 mg L^{-1}, indicating enhanced capacitive behavior driven by increased carrier density and interfacial polarization (Figure.15(A)). The corresponding M″ spectra exhibit a concentration-dependent shift in relaxation processes (Figure.15(B)). At low concentration (1 mg L^{-1}), a sharp rise in the high-frequency domain reflects rapid ionic relaxation, whereas higher loading (10 mg L^{-1})

induces slower polarization dynamics, suggesting that excessive incorporation of CNDs promotes space-charge accumulation and delayed relaxation. In the case of ZnO NP treatment, the concentration-dependent response is non-linear. The highest M′ values are recorded at 5 mg L^{-1} across the frequency range (Figure.15(C)), reflecting an optimal balance between charge transport and dielectric confinement. At 10 mg L^{-1}, the modulus response declines, likely due to nanoparticle aggregation or restricted conduction pathways. The M″ spectra further corroborate this observation (Figure.15(D)), with pronounced relaxation peaks at 1 and 10 mg L^{-1}, while 5 mg L^{-1} maintains a comparatively stable conduction-relaxation process.

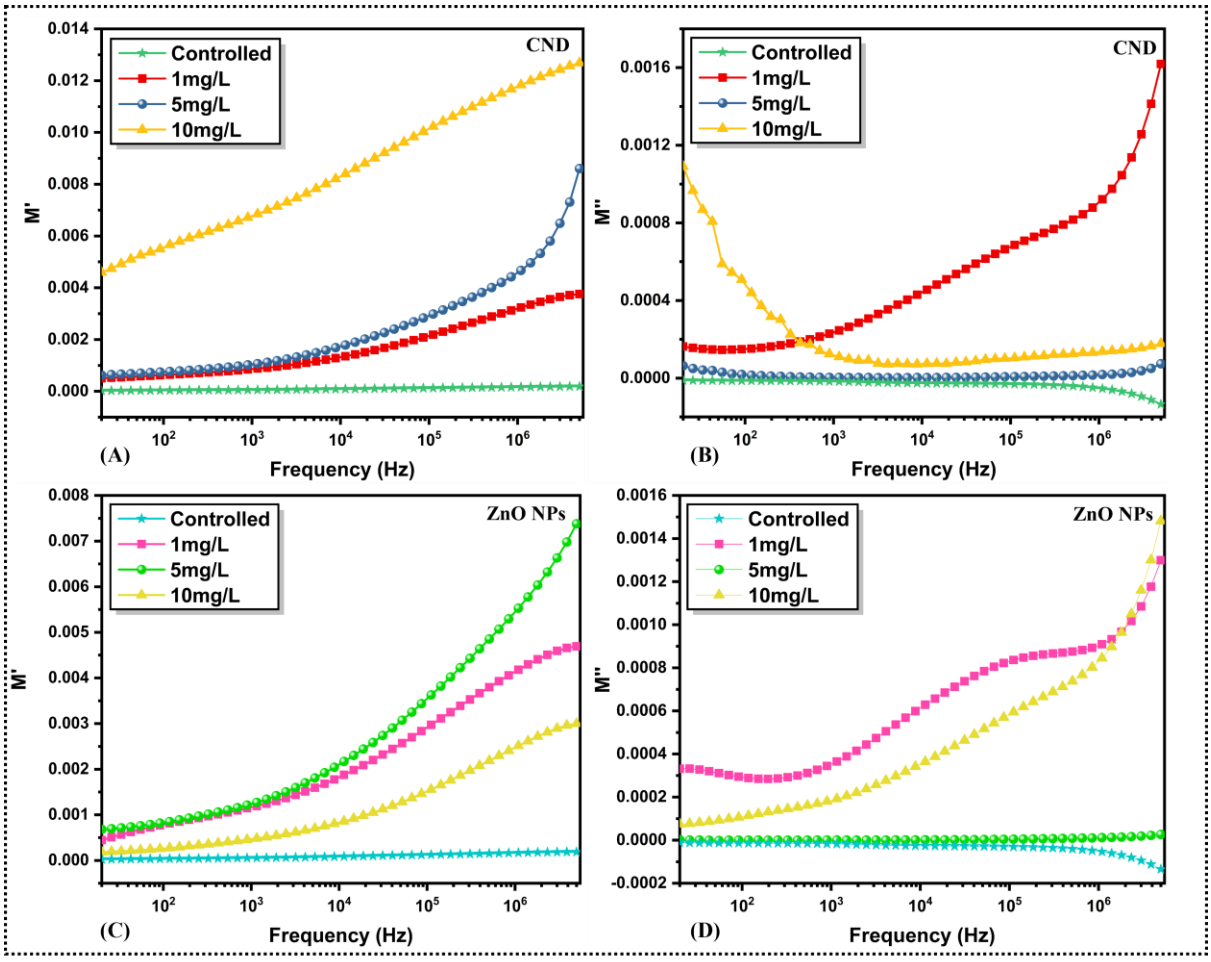

Figure.15 *Electric modulus spectra of jade plants treated with CNDs and ZnO nanoparticles. CND treatment (A-B) shifts both M' and M" toward higher values with increasing dose, but at 10 mg L^{-1} the spectra flatten, reflecting constrained relaxation and limited charge mobility. By contrast, ZnO NPs (C–D) produce a graded rise in M' and M" across concentrations, with 5 mg L^{-1} showing the strongest dispersion, while 10 mg L^{-1} moderates the response, indicative of altered space-charge polarization.*

The M′ - M″ spectra of jade plants revealed distinct yet converging trends under CND and ZnO NP exposure, providing mechanistic insights into how nanomaterials modulate ionic transport and relaxation in biological tissues (Figure.16 and Figure.17).

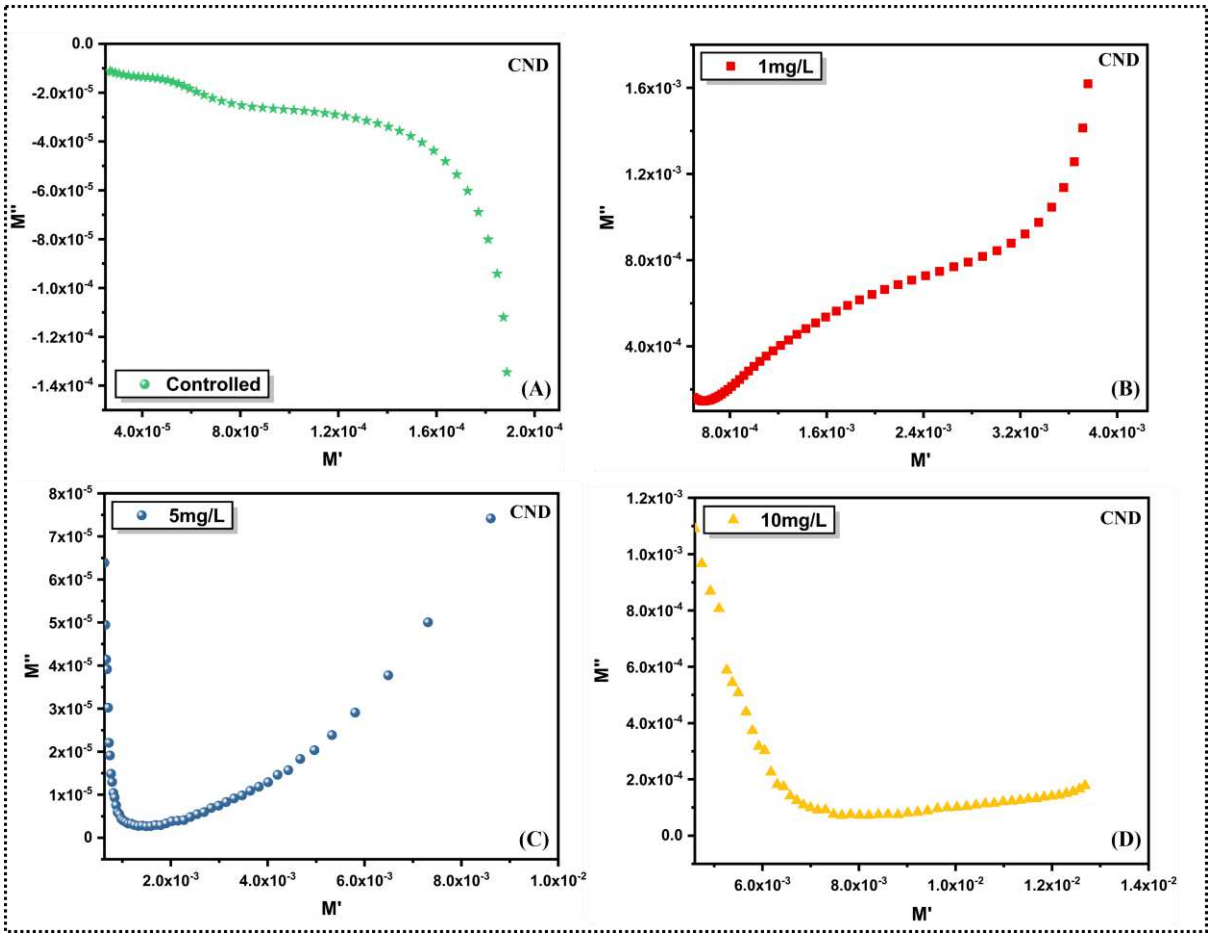

Figure 16. *Electric modulus spectra (M' vs M") of Crassula ovata exposed to carbon nanodots. CNDs induced a systematic shift in the complex modulus with concentration, marked by rising M' and M" values and gradual suppression of relaxation peaks. The narrowing of arcs at higher doses reflects hindered ionic mobility and increased rigidity of interfacial regions, consistent with progressive blocking of conduction pathways.*

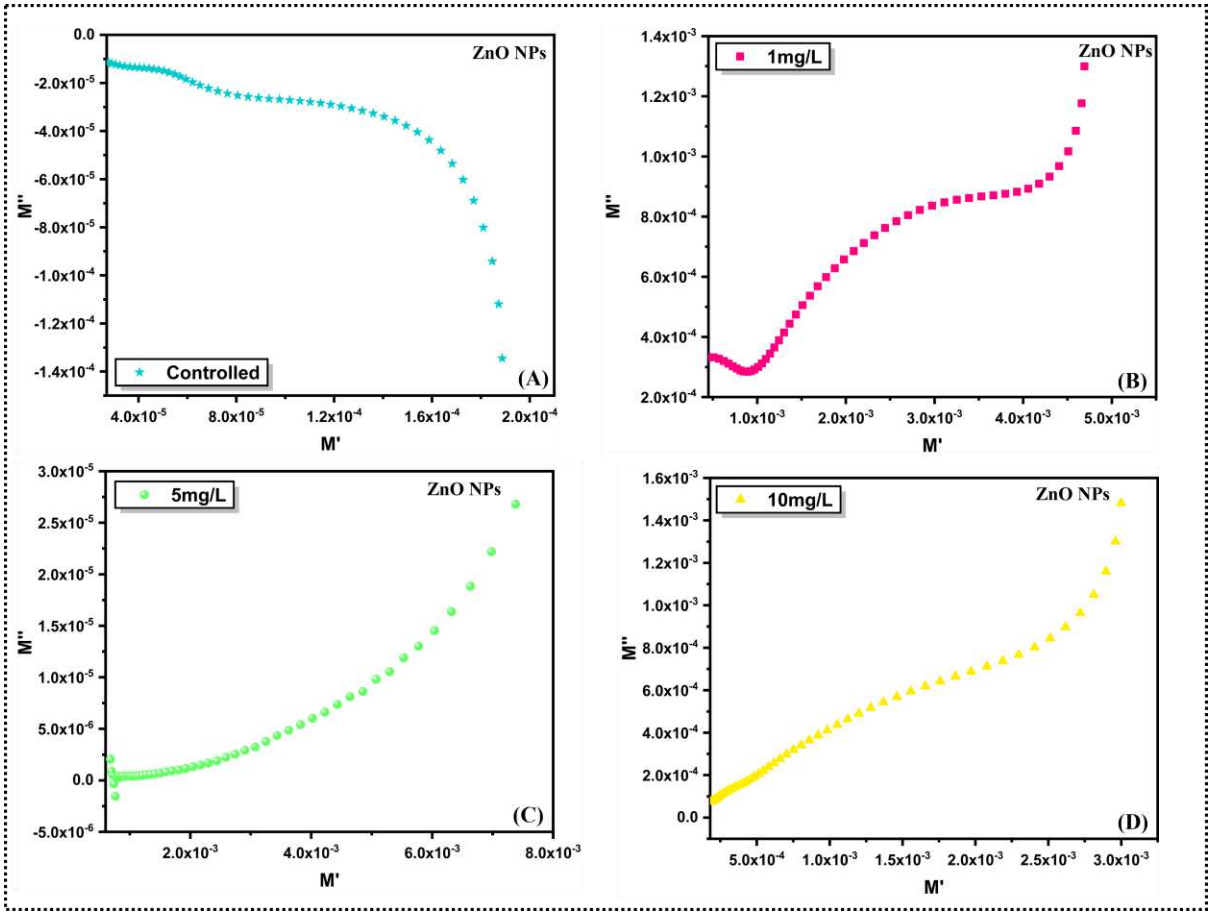

Figure 17. *Electric modulus spectra (M′ vs M″) of Crassula ovata exposed to ZnO nanoparticles. ZnO NPs altered the relaxation dynamics in a concentration-dependent manner. At 5 mg L^{-1}, sharper modulus peaks and shifted arcs indicated restricted transport and enhanced interfacial polarization, while at 10 mg L^{-1}, the broadening of features suggested partial recovery of conduction through Zn^{2+}-mediated defect pathways.*

Untreated controls in both cases exhibited negligible M′ and M″ values, reflecting the intrinsically resistive nature of jade plant tissues and the absence of pronounced dielectric relaxation. Upon nanoparticle exposure, however, divergent responses emerged depending on material composition and concentration. At low concentration (1 mg L^{-1}), both CNDs and ZnO NPs produced a pronounced elevation in M′ and M″, indicative of enhanced ionic mobility and accelerated dielectric relaxation. This enhancement is likely driven by the nanoparticles ability to interact with cellular interfaces, reducing resistive barriers and promoting space-charge polarization[58]. In the case of CNDs (Figure.16(B)), this effect can be attributed to their high surface functionalization and capacity to form transient conduction pathways[59]. ZnO NPs (Figure.17(B)) facilitate relaxation through surface hydroxyl groups and the release of Zn^{2+} ions, which promote defect-mediated hopping and enhance interfacial polarization[60] across plant membranes.

As concentrations increased, the trajectories diverged. For CNDs, progressive agglomeration at 5 and 10 mg L^{-1} (Figure.16(C)and 16(D)) led to a suppression of relaxation, as conduction pathways became increasingly obstructed and interfacial resistance dominated the response. In contrast, ZnO NPs exhibited a biphasic profile: while 5 mg L^{-1} caused partial suppression due to localized trapping (Figure.17(C)), at 10 mg L^{-1} the system recovered with a strong modulus response (Figure.17(D)), consistent with extensive space-charge accumulation and percolation of interfacial regions that override aggregation-induced constraints.

4. Conclusion

This study demonstrates that carbon nanodots (CNDs) and zinc oxide (ZnO) nanoparticles induce fundamentally distinct electrochemical modifications in *Crassula ovata*. Impedance spectroscopy revealed that CNDs produce a monotonic, concentration-dependent suppression of ionic mobility, manifested as progressively higher grain boundary resistance and reduced dielectric permittivity. These changes point to direct obstruction of conduction pathways, with compensatory polarization effects arising from space-charge accumulation. In contrast, ZnO NPs elicit a biphasic response at moderate concentrations (5 mg L^{-1}) they strongly restrict charge transport, whereas at higher concentrations (10 mg L^{-1}) partial recovery of conductivity and dielectric relaxation occurs through Zn^{2+}-mediated modulation of membrane permeability and defect-assisted polarization. Interestingly, a comparable concentration-dependent saturation behavior has been observed in our earlier and ongoing studies on *Aloe vera* treated with Nickel cobalt carbonate hydroxide[33] and ZnO nanomaterials, where beyond an optimal concentration (~5 mg L^{-1}), plants exhibit limited nanoparticle uptake and stabilization of impedance parameters. This recurrent trend across distinct plant systems suggests the existence of a physiological threshold beyond which nanoparticle assimilation is actively restricted, preserving ionic equilibrium within tissues.

The divergence between these two nanomaterials underscores the critical role of nanoparticle chemistry in dictating plant electrochemical responses. While both CNDs and ZnO NPs alter interfacial polarization and conduction pathways, CNDs drive a unidirectional trend toward resistive and non-ideal capacitive behavior, whereas ZnO NPs engage dynamic physiological adaptations that balance ionic restriction with defect-enabled transport. This mechanistic contrast highlights a broader principle in plant nanobionics: carbon-based nanostructures primarily act as physical modulators of conduction, while metal oxides function as chemical regulators of ionic homeostasis. By establishing this distinction, our work provides a framework for

rational selection of nanomaterials in plant-based bioelectronic systems. Understanding how material composition governs ionic dynamics not only advances fundamental plant electrophysiology but also informs the design of future biohybrid interfaces for sensing, energy harvesting, and sustainable electronic applications.

Acknowledgment: The authors express their sincere gratitude to the Research and Development Department, UPES Dehradun, for providing the necessary research infrastructure and facilities to carry out this work. The authors also acknowledge UPES University for providing Junior Research Fellowships (JRF) to Kajal and Mohit, which greatly supported this research.

Author Contributions: K.G. conceptualized the study, conducted the experimental work and characterization, compiled and analyzed the data, and prepared the original draft of the manuscript. **M.B.** contributed to the experimental work, data analysis, characterization, and critically reviewed and edited the manuscript. **A.S.** and **H.S.** contributed to the review and editing of the manuscript. **A.K.S.** supervised the overall work, provided project administration, guided data analysis, and reviewed and edited the manuscript.

Ethics declarations: The authors declare no competing interests.

Data availability- The datasets used and/or analysed during the current study available from the corresponding author on reasonable request.

References:

1. Barbinta-Patrascu, M.-E., Bita, B. & Negut, I. From nature to technology: exploring the potential of plant-based materials and modified plants in biomimetics, bionics, and green innovations. *Biomimetics* **9**, 390 (2024).
2. Li, R. *et al.* Electrical and calcium signaling in plant systemic defense: from local wounds to global responses. *New Phytol.* **247**, 1633–1642 (2025).
3. Bianchi, M. *et al.* Temporal Dynamics With and Without a Nervous System: Plant Physiology, Communication, and Movement. *Cogn. Sci.* **49**, e70079 (2025).

4. Dufil, G., Bernacka-Wojcik, I., Armada-Moreira, A. & Stavrinidou, E. Plant bioelectronics and biohybrids: the growing contribution of organic electronic and carbon-based materials. *Chem. Rev.* **122**, 4847–4883 (2021).
5. Balachandran, A., Parayilkalapurackal, H., Rajpoot, S. & Lone, S. Bioinspired Green Fabricating Design of Multidimensional Surfaces for Atmospheric Water Harvesting. *ACS Appl. Bio Mater.* **6**, 44–63 (2023).
6. Nikolic, M. V., Singh, C. & Bogdanovic, M. Exploration of the charge transport mechanism, complex impedance, dielectric/electric modulus and energy storage characteristics of the aloe vera (Aloe Barbadensis Miller) plant. *Mater. Res. Express* **11**, 016302 (2024).
7. Liu, J. *et al.* Plant nanobiotechnology: a new strategy to enhance crop photosynthesis. *Env. Sci Nano* **11**, 4655–4665 (2024).
8. Gautam, K., Bhatt, M., Dutt, S., Sagdeo, A. & Sinha, A. K. Impact of carbon nanodot uptake on complex impedance charge transport and energy storage mechanism in aloe vera leaves. *Sci. Rep.* **15**, 11506 (2025).
9. Perfileva, A. I. & Krutovsky, K. V. Manganese nanoparticles: synthesis, mechanisms of influence on plant resistance to stress, and prospects for application in agricultural chemistry. *J. Agric. Food Chem.* **72**, 7564–7585 (2024).
10. Cameron, S. J., Sheng, J., Hosseinian, F. & Willmore, W. G. Nanoparticle effects on stress response pathways and nanoparticle–protein interactions. *Int. J. Mol. Sci.* **23**, 7962 (2022).
11. Fallah, S., Yusefi-Tanha, E. & Peralta-Videa, J. R. Interaction of nanoparticles and reactive oxygen species and their impact on macromolecules and plant production. *Plant Nano Biol.* **10**, 100105 (2024).
12. Gautam, K., Bhatt, M., Sagdeo, A., Singh, H. & Sinha, A. K. Charge transport dynamics and energy storage implications of nickel cobalt carbonate hydroxide interaction with the Aloe vera leaf matrix. *Nanoscale Adv.* (2025).
13. Elmer, W., Hines, D. & Schultes, N. P. First report of Fusarium libertatis causing vascular disease of Jade plant (Crassula ovata). *J. Plant Pathol.* **105**, 1207–1208 (2023).

14. Jones, L. A. Anatomical adaptations of four Crassula species to water availability. *Biosci. Horiz. Int. J. Stud. Res.* **4**, 13–22 (2011).

15. LÜTTGE, U. Ecophysiology of Crassulacean Acid Metabolism (CAM). *Ann. Bot.* **93**, 629–652 (2004).

16. Ali, J., Ali, N., Wang, L., Waseem, H. & Pan, G. Revisiting the mechanistic pathways for bacterial mediated synthesis of noble metal nanoparticles. *J. Microbiol. Methods* **159**, 18–25 (2019).

17. Zaman, W., Ayaz, A. & Park, S. Nanomaterials in Agriculture: A Pathway to Enhanced Plant Growth and Abiotic Stress Resistance. *Plants* **14**, 716 (2025).

18. Munyaneza, V. *et al.* Mitigating Metal Toxicity in Plants Using Nanoparticles: Mechanisms and Implications for Sustainable Agriculture. *J. Agric. Food Chem.* **73**, 17374–17386 (2025).

19. Gautam, K., Singh, H. & Sinha, A. Nanotechnology in Plant Nanobionics: Mechanisms, Applications, and Future Perspectives. *Adv. Biol.* **9**, 2400589 (2025).

20. Ali, S., Mehmood, A. & Khan, N. Uptake, Translocation, and Consequences of Nanomaterials on Plant Growth and Stress Adaptation. *J. Nanomater.* **2021**, 6677616 (2021).

21. Mony, C. *et al.* Nanomaterials for enhancing photosynthesis: interaction with plant photosystems and scope of nanobionics in agriculture. *Environ. Sci. Nano* **9**, 3659–3683 (2022).

22. Zhao, L. *et al.* Nano-Biotechnology in Agriculture: Use of Nanomaterials to Promote Plant Growth and Stress Tolerance. *J. Agric. Food Chem.* **68**, 1935–1947 (2020).

23. Minervini, G. *et al.* Exploring carbon dots: Green nanomaterials for unconventional lasing. *Small* **20**, 2403653 (2024).

24. Qiu, C., Jiang, L., Gao, Y. & Sheng, L. Effects of oxygen-containing functional groups on carbon materials in supercapacitors: A review. *Mater. Des.* **230**, 111952 (2023).

25. Bhatt, M., Gautam, K., Verma, A. & Sinha, A. K. Structural, Optical, Surface Chemical, and Electrochemical Characterization of Aloe Vera-Assisted ZnO Nanostructures for Supercapattery Applications. *Mater. Adv.* 10.1039.D5MA00556F (2025) doi:10.1039/D5MA00556F.

26. Bhatt, M. Green synthesis of Aloe vera-assisted Co3O4 nanostructures: structural, electronic, optical, and electrochemical insights for supercapattery applications. **15**, 28626–28641 (2025).

27. Uma, J., Banumathi, S., Maheswaran, R., Senthilkumar, N. & Balraj, B. Green Synthesis of ZnMn2O4 Nanoparticles for Supercapacitor Applications. *J. Supercond. Nov. Magn.* **34**, 817–823 (2021).

28. Kim, S. H., Bae, S., Sung, Y. W. & Hwang, Y. S. Effects of particle size on toxicity, bioaccumulation, and translocation of zinc oxide nanoparticles to bok choy (Brassica chinensis L.) in garden soil. *Ecotoxicol. Environ. Saf.* **280**, 116519 (2024).

29. Wei, S. Uptake And Translocation Of ZnO Nanoparticles In Rice Tissues Studied By Single Particle-ICP-MS. *At. Spectrosc.* **44**, 343–353 (2023).

30. Wu, P. *et al.* Dissolution and Transformation of ZnO Nano- and Microparticles in Soil Mineral Suspensions. *ACS Earth Space Chem.* **3**, 495–502 (2019).

31. Paul, P. *et al.* Crystallographic facet engineering of ZnO nanoparticles for photocatalytic organic pollutant degradation and antibacterial activity. *Mater. Adv.* **6**, 4696–4704 (2025).

32. Strekalovskaya, E. I., Perfileva, A. I. & Krutovsky, K. V. Zinc Oxide Nanoparticles in the "Soil–Bacterial Community–Plant" System: Impact on the Stability of Soil Ecosystems. *Agronomy* **14**, 1588 (2024).

33. Gautam, K., Bhatt, M., Sagdeo, A., Singh, H. & Sinha, A. K. Charge Transport Dynamics and Energy Storage Implications of Nickel Cobalt Carbonate Hydroxide Interaction with Aloe Vera Leaf Matrix. *Nanoscale Adv.* 10.1039.D5NA00651A (2025) doi:10.1039/D5NA00651A.

34. Li, H., Kang, Z., Liu, Y. & Lee, S.-T. Carbon nanodots: synthesis, properties and applications. *J. Mater. Chem.* **22**, 24230–24253 (2012).

35. Zhang, Q., Wang, R., Feng, B., Zhong, X. & Ostrikov, K. Photoluminescence mechanism of carbon dots: triggering high-color-purity red fluorescence emission through edge amino protonation. *Nat. Commun.* **12**, 6856 (2021).

36. Wang, L. *et al.* Common Origin of Green Luminescence in Carbon Nanodots and Graphene Quantum Dots. *ACS Nano* **8**, 2541–2547 (2014).

37. Chen, D. *et al.* Excitation-independent dual-color carbon dots: surface-state controlling and solid-state lighting. *Acs Photonics* **4**, 2352–2358 (2017).

38. Zu, F. *et al.* The quenching of the fluorescence of carbon dots: a review on mechanisms and applications. *Microchim. Acta* **184**, 1899–1914 (2017).

39. van Dijken, A., Meulenkamp, E. A., Vanmaekelbergh, D. & Meijerink, A. The luminescence of nanocrystalline ZnO particles: the mechanism of the ultraviolet and visible emission. *J. Lumin.* **87–89**, 454–456 (2000).

40. Apostoluk, A. *et al.* Improved visible emission from ZnO nanoparticles synthesized via the Co-precipitation method. *Materials* **16**, 5400 (2023).

41. Banger, A. *et al.* Synthetic Methods and Applications of Carbon Nanodots. *Catalysts* **13**, (2023).

42. Mohammed, S. J., Omer, K. M. & Hawaiz, F. E. Deep insights to explain the mechanism of carbon dot formation at various reaction times using the hydrothermal technique: FT-IR, 13 C-NMR, 1 H-NMR, and UV-visible spectroscopic approaches. *RSC Adv.* **13**, 14340–14349 (2023).

43. Sonowal, A. *et al.* Citrus aurantifolia-derived carbon quantum dots with red fluorescence emission for codelivery with curcumin as theranostic liposomes for lung cancer. *Future J. Pharm. Sci.* **10**, 116 (2024).

44. Noei, H. *et al.* The identification of hydroxyl groups on ZnO nanoparticles by infrared spectroscopy. *Phys. Chem. Chem. Phys.* **10**, 7092 (2008).

45. Kołodziejczak-Radzimska, A. & Jesionowski, T. Zinc Oxide—From Synthesis to Application: A Review. *Materials* **7**, 2833–2881 (2014).

46. Djurišić, A. B. & Leung, Y. H. Optical Properties of ZnO Nanostructures. *Small* **2**, 944–961 (2006).

47. Spanhel, L. & Anderson, M. A. Semiconductor clusters in the sol-gel process: quantized aggregation, gelation, and crystal growth in concentrated zinc oxide colloids. *J. Am. Chem. Soc.* **113**, 2826–2833 (1991).

48. Jebli, M., Rayssi, Ch., Dhahri, J. & Ben Henda, M. Frequency-temperature response of Ba0.97La0.02Ti0.95Nb0.04O3 ceramic prepared by molten-salt method: impedance and modulus spectroscopy characterization. *J. Mater. Sci. Mater. Electron.* **32**, 26786–26797 (2021).

49. Hajra, S., Sahu, M., Purohit, V. & Choudhary, R. N. P. Dielectric, conductivity and ferroelectric properties of lead-free electronic ceramic:0.6Bi(Fe0.98Ga0.02)O3-0.4BaTiO3. *Heliyon* **5**, e01654 (2019).

50. Sahu, M., Hajra, S., Mohanta, K., Purohit, V. & Choudhary, R. N. P. Dielectric and impedance spectroscopy of aluminium oxide substituted fused silica samples. *SN Appl. Sci.* **1**, 1254 (2019).

51. Gateman, S. M. *et al.* On the use of a constant phase element (CPE) in electrochemistry. *Curr. Opin. Electrochem.* **36**, 101133 (2022).

52. Balaguera, E. H. & Allagui, A. Limit capacitance of the constant phase element. *J. Energy Storage* **90**, 111801 (2024).

53. Gong, Z. *et al.* Influence of grain boundary and grain size on the mechanical properties of polycrystalline ceramics: grain-scale simulations. *J. Am. Ceram. Soc.* **103**, 5900–5913 (2020).

54. Defferriere, T., Klotz, D., Gonzalez-Rosillo, J. C., Rupp, J. L. & Tuller, H. L. Photo-enhanced ionic conductivity across grain boundaries in polycrystalline ceramics. *Nat. Mater.* **21**, 438–444 (2022).

55. Hona, R. K., Dhaliwal, G. S. & Thapa, R. Investigation of Grain, Grain Boundary, and Interface Contributions on the Impedance of Ca2FeO5. *Appl. Sci.* **12**, (2022).

56. Brantlov, S. *et al.* Cell Membrane Capacitance (Cm) Measured by Bioimpedance Spectroscopy (BIS): A Narrative Review of Its Clinical Relevance and Biomarker Potential. *Sensors* **25**, (2025).

57. Lazanas, A. Ch. & Prodromidis, M. I. Electrochemical Impedance Spectroscopy─A Tutorial. *ACS Meas. Sci. Au* **3**, 162–193 (2023).

58. Xu, H. *et al.* Interfacial Storage for Next-Generation Batteries: Mechanisms, Advances, and Challenges. *Carbon Neutralization* **4**, e70031 (2025).

59. Cadranel, A., Margraf, J. T., Strauss, V., Clark, T. & Guldi, D. M. Carbon Nanodots for Charge-Transfer Processes. *Acc. Chem. Res.* **52**, 955–963 (2019).

60. Kumar, S. G. & Rao, K. K. Zinc oxide based photocatalysis: tailoring surface-bulk structure and related interfacial charge carrier dynamics for better environmental applications. *Rsc Adv.* **5**, 3306–3351 (2015).